

Direct reduction of iron-ore with hydrogen in fluidized beds: A coarse-grained CFD-DEM-IBM study

Bin Lan^{a,b}, Ji Xu^{b,c}, Shuai Lu^{b,c}, Yige Liu^{b,c}, Fan Xu^{a,b}, Bidan Zhao^{b,c}, Zheng Zou^{b,c}, Ming Zhai^{a,*}, Junwu Wang^{b,c,d,*}

^a*School of Energy Science and Engineering, Harbin Institute of Technology, Harbin, 150001, P. R. China*

^b*State Key Laboratory of Multiphase Complex Systems, Institute of Process Engineering, Chinese Academy of Sciences, P. O. Box 353, Beijing 100190, P. R. China*

^c*School of Chemical Engineering, University of Chinese Academy of Sciences, Beijing, 100049, P. R. China*

^d*Innovation Academy for Green Manufacture, Chinese Academy of Sciences, Beijing, 100190, P. R. China*

Abstract

Hydrogen metallurgy technology uses hydrogen as the reducing agent instead of carbon reduction, which is one of the important ways to reduce carbon dioxide emissions and ensure the green and sustainable development of iron and steel industry. Due to the advantages of high gas-solid contact efficiency and outstanding mass and heat transfer, direct reduction of iron ore in fluidized beds has attracted much attention. In this study, a coarse-grained CFD-DEM-IBM solver based on hybrid CPU-GPU computing is developed to simulate the direct reduction process of two kinds of iron ore with hydrogen in fluidized beds, where an unreacted shrinking core model based on multiple reaction paths is used to model the reduction reactions, a coarse-grained model and multiple GPUs enable the significant acceleration of particle computation, and the immersed boundary method (IBM) enables the use of simple mesh even in complex geometries of reactors. The predicted results of particle reduction degree are in good agreement with the experimental values, which proves the correctness of the CFD-DEM-IBM solver. In addition, the effects of reaction kinetic parameters and operating temperature on particle reduction degree are also investigated. Present study provides a method for digital design, optimization and scale-up of ironmaking reactors.

Keywords: Direct reduction; Fluidization; CFD-DEM; Unreacted shrinking core model; Coarse-graining

1. Introduction

The steel industry has played a great role in supporting and promoting national defense, petroleum, shipbuilding, buildings, and equipment manufacturing [1]. Metallic iron, as one of the main components of steel, can generally be produced by three process routes [2]: blast furnace, direct reduction and smelting reduction. At present, due to the advantages of mature technology and high output, blast furnace ironmaking is the dominant process in steel production [3]. However, the production process of blast furnace ironmaking is complicated, and the carbon dioxide and sulfur dioxide emissions generated after the combustion of the coke used in smelting are very high, which causes serious pollution to the environment [4]. In order to alleviate the pressure of ironmaking on environment, resource and energy, non-blast furnace technology has been paid more and more attention by researchers [5, 6, 7]. Non-blast furnace ironmaking completely get rid of the dependence on coke and realize the comprehensive utilization of complex symbiotic iron ore resources while meeting the requirements of environmental protection.

As a typical non-blast furnace ironmaking method, fluidized ironmaking directly uses pulverized ore as raw material, which eliminates the process of pelletizing and sintering and helps to realize the efficient utilization of low-grade complex iron ore [8]. The direct reduction of iron ore in fluidized beds is a promising method for iron making because of its high heat and mass transfer efficiency and rapid reduction rate [9]. The world's first Fluid Iron Ore Reduction (FIOR) process appeared in 1960 and was commercially operated in Venezuela in 1976 until it was shut down in 2000

*Corresponding author

Email addresses: zhaiming@hit.edu.cn (Ming Zhai), jwwang@ipe.ac.cn (Junwu Wang)

[10]. After that, various iron and steel enterprises successively established FINMET, FINEX, Circored, Circofer and other processes [11]. These processes have one thing in common, that is, the fluidized reduction system is generally composed of two or more fluidized bed reactors in series, and the gas and particles are in countercurrent contacting state. The advantages of this design lie in the fact that it can make full use of the waste heat of reducing gas to preheat iron ore powder to speed up the reaction rate, to reduce the consumption of reducing gas and to improve the gas utilization rate [12]. Many researchers have conducted experimental studies on the hydrodynamics and reaction mechanism in fluidized bed for iron ore reduction [13, 14, 15, 16, 17, 18, 19, 20, 21]. It was found that fine iron ore powder (about 100 μm) is easy to stick together when reduced at high temperature [22], thus forming clusters and depositing at the bottom of the bed, and finally resulting in the occurrence of defluidization. Adhesion and defluidization can be effectively inhibited by granulation [18], solid additive coating [23], carbon deposition-reduction [24], reducing reduction temperature [25], and/or increasing operating gas velocity [26]. The use of pure hydrogen as a reducing agent to make iron is known as hydrogen metallurgy, and this technology has attracted much attention in recent years due to its ability to achieve CO₂ emission reduction targets [27, 28, 29].

In addition to experiment, numerical simulation has gradually become an important means to study the direct reduction of iron ore [30, 31, 32, 33, 34, 35, 36, 37, 38, 39, 40]. Among many numerical calculation methods for reduction reaction, CFD-DEM method is popular. The DEM model can provide information of force, velocity, position, temperature, reaction rate and other important data on the particle scale, which are difficult to obtain by experiment. Therefore, DEM simulation is extremely helpful for researchers and engineers to understand the hydrodynamics, heat and mass transfer as well as chemical reaction characteristics of particles in the reactor. Natsui [33] adopted CFD-DEM method to simulate the process of direct reduction of large hematite particles (with a particle size of 4 cm) to iron in three-dimensional packed bed, and observed that the heterogeneity of the reaction rate and the temperature distribution was affected by particle arrangement. Dianyu [41] found that with the increase of operating pressure (below 5 atm), the reduction rate of single hematite pellet increased significantly, and the entire reduction process under non-isothermal conditions was slower than that under isothermal conditions. Xu [42] used a coarse-grained CFD-DEM model to study the simplified reduction reaction of iron ore accompanied by coke gasification in blast furnaces. In the gas-solid chemical reaction, the particles may shrink or expand, and their surfaces may form an outer layer of solid products. Shrinkage/expansion in a reaction is often described by the shrinking core model (SCM) and the unreacted core model (UCM) [43]. In iron ore reduction reactions, these two phenomena complement each other and are represented by the unreacted shrinking core model (USCM) [31]. Kinaci [44, 36, 37] combined the USCM reaction rate model with the CFD-DEM method, and simulated the reduction reaction of centimeter-level iron ore particles.

Although the USCM model has been widely used in numerical studies of reaction flows, a complete resistance network (reaction path) that considers the effects of particle structure, reduction gas concentration, and reaction temperature during the reaction has not been found in the literature. The reduction resistance network is directly related to the reaction resistance and thus affects the reaction rate. Therefore, the accurate construction of mathematical and physical models of iron ore direct reduction is the key to predict the hydrodynamics, mass transfer and heat transfer behavior of gas and solid in the reactor based on CFD-DEM method. In this study, the USCM model is coupled to a coarse-grained CFD-DEM method, where the motions of gas phase and of iron ore particles are described by the continuum model and the soft sphere model, respectively. Immersed boundary method (IBM), which enables the use of Cartesian meshes for complex geometries of reactors, is coupled to CFD-DEM method. This can conveniently implement the boundary conditions of velocity, pressure, temperature and gas composition. At the same time, the pseudo-turbulence models for hydrodynamic, heat and mass transfer are closed using correlations that are generated from particle-resolved direct numerical simulations. In addition to the application of coarse-grained method, the calculation of particles is GPU-based, and the calculation speed of solid phase is significantly accelerated. The kinetic parameter of the reaction (pre-exponential factor) is determined by means of experimental data correction rather than directly from the literature. The reduction process of two different kinds of iron ore in bubbling bed is simulated, and the effects of kinetic parameters and operating temperature on the reduction degree, reaction resistance and porosity of particles are investigated. The rest of the article is organized as follows: Section 2 introduces the reaction model. The CFD-DEM governing equations and constitutive relations are given in Section 3. Section 4 shows numerical method and simulation setup. In Section 5, the simulation results are analyzed and the reduction degree are compared with the experimental data available in literature. The conclusions are drawn in Section 6.

Table 1: Hematite reduction by steps [47].

Reaction	ΔH	Equation
$3\text{Fe}_2\text{O}_3 + \text{H}_2 \rightarrow 2\text{Fe}_3\text{O}_4 + \text{H}_2\text{O}$	<0	R1
$\text{Fe}_3\text{O}_4 + \text{H}_2 \rightarrow 3\text{FeO} + \text{H}_2\text{O}$	>0	R2
$\text{FeO} + \text{H}_2 \rightarrow \text{Fe} + \text{H}_2\text{O}$	>0	R3

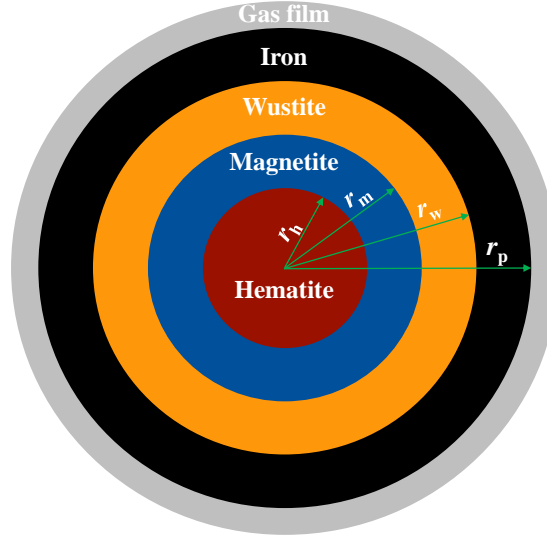


Figure 1: Schematic illustration of three-layer USC (r_p is particle radius, r_h , r_m and r_w are the radius of core, product layer m and w, respectively).

2. Reaction model

Hematite (Fe_2O_3) can be gradually reduced to magnetite (Fe_3O_4), wustite (FeO) and iron (Fe) in H_2 atmosphere when the reaction temperature is above 570°C [45]. It can be seen from Table 1 that the reaction of Fe_2O_3 to Fe_3O_4 in the hydrogen atmosphere is exothermic, Fe_3O_4 to FeO and FeO to Fe are endothermic, so continuous heat input is required to ensure the normal reduction of hematite. In the three-layer USC, the particles consist of unreacted hematite core, product layers (magnetite, wustite and metallic iron), and gas film (Figure 1). Based on this model, the following assumptions are made: (i) Each sub-reaction is a first order irreversible reaction; (ii) The radius of the particle does not change, but the structure changes during the whole reduction process; (iii) The sintering effect is not considered, and the structural changes are only caused by chemical reactions; (iv) The temperature inside the particle is uniform because the particles are small; (v) Catalysis and side reactions are ignored. The reduction process of iron ore is considered to be a resistance network [46] (Figure 2), which represents three rate control steps, namely, mass transfer resistance F through the gas film layer, diffusion resistance B through the product layer and chemical reaction resistance A at the reaction interface. The mass change rate of the reacting gas can be expressed by the resistance mentioned above by using the Kirchoff's law [46].

2.1. Reaction rate model: the raw iron ore is hematite

The rate of mass change of reducing gas (H_2) in reaction $k \rightarrow l$ is [31]:

$$\dot{m}_j^{kl} = \frac{\eta_j^{kl} A_{pi}}{T_{pi}} \frac{M_j p_g}{R_g} \left[v_1^{kl} (x_j - x_{eq,j}^{hm}) + v_2^{kl} (x_j - x_{eq,j}^{mw}) + v_3^{kl} (x_j - x_{eq,j}^{wFe}) \right]_j, \quad (1)$$

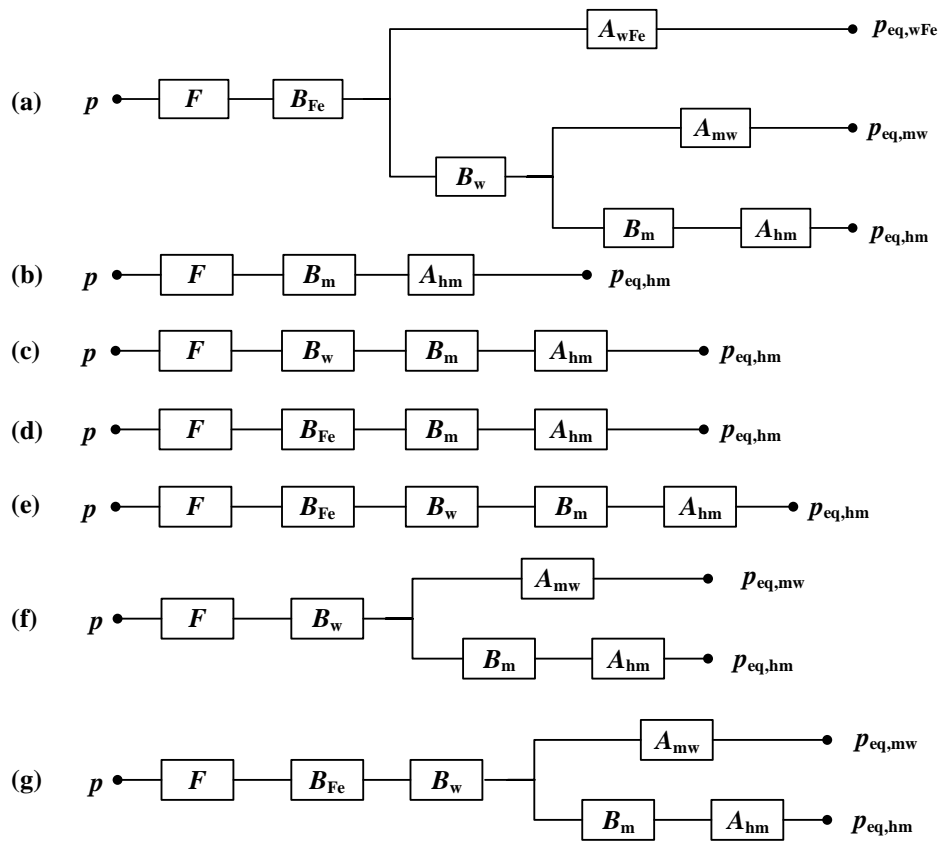


Figure 2: Resistance network for progressive reduction of hematite (p is the gas pressure, F represents the mass transfer resistance through the gas film layer, B represents the diffusion resistance through the product layer and A represents the chemical reaction resistance at the reaction interface. Furthermore, h, m and w represent hematite, magnetite and wustite, respectively).

where k and l represent solid reactant (Fe_2O_3 , Fe_3O_4 or FeO) and product (Fe_3O_4 , FeO or Fe) in each sub-reaction, respectively. Subscript j represents reducing gas, and A_{pi} and T_{pi} are the surface area and temperature of particle pi , respectively. p_g is the gas pressure of the grid where the particle pi is located, and R_g is the gas constant (8.314 J/mol/K). M_j and η_j are the molar mass and stoichiometric coefficients of the gas, respectively. Note that for H_2 , the mole fraction $x_{\text{H}_2} = x'_{\text{H}_2} / (x'_{\text{H}_2} + x'_{\text{H}_2\text{O}})$, where x'_{H_2} , $x'_{\text{H}_2\text{O}}$ respectively represent the true mole fraction of each species in the gas phase (N_2 might be in the gas phase). The mole fraction is calculated by the mass fraction:

$$x'_j = Y_j M_g / M_j, \quad (2)$$

$$M_g = \left(\sum Y_j / M_j \right)^{-1}, \quad (3)$$

where M_g is the average molar mass of the gas mixture, and Y_j is the mass fraction of the gas j . x_{eq} is the mole fraction of reducing gas at reaction equilibrium, and its relationship with equilibrium constant K_{eq} is as follows:

$$x_{\text{eq},j}^{kl} = 1 / (K_{\text{eq}}^{kl} + 1). \quad (4)$$

For the three-layer USCM, according to the reaction resistance network in Figure 2 (a), the resistance coefficients v_1^{kl} , v_2^{kl} and v_3^{kl} can be derived as follows:

$$v_1^{\text{hm}} = [A_{\text{wFe}} (A_{\text{mw}} + B_{\text{w}} + B_{\text{Fe}} + F) + (B_{\text{Fe}} + F) (A_{\text{mw}} + B_{\text{w}})] / W, \quad (5)$$

$$v_2^{\text{hm}} = -[A_{\text{wFe}} (B_{\text{w}} + B_{\text{Fe}} + F) + B_{\text{w}} (B_{\text{Fe}} + F)] / W, \quad (6)$$

$$v_3^{\text{hm}} = -A_{\text{mw}} (B_{\text{Fe}} + F) / W, \quad (7)$$

$$v_1^{\text{mw}} = -[B_{\text{w}} (A_{\text{wFe}} + B_{\text{Fe}} + F) + A_{\text{wFe}} (B_{\text{Fe}} + F)] / W, \quad (8)$$

$$v_2^{\text{mw}} = [(A_{\text{hm}} + B_{\text{m}} + B_{\text{w}}) (A_{\text{wFe}} + B_{\text{Fe}} + F) + A_{\text{wFe}} (B_{\text{Fe}} + F)] / W, \quad (9)$$

$$v_3^{\text{mw}} = -(A_{\text{hm}} + B_{\text{m}}) (B_{\text{Fe}} + F) / W, \quad (10)$$

$$v_1^{\text{wFe}} = -A_{\text{mw}} (B_{\text{Fe}} + F) / W, \quad (11)$$

$$v_2^{\text{wFe}} = -(A_{\text{hm}} + B_{\text{m}}) (B_{\text{Fe}} + F) / W, \quad (12)$$

$$v_3^{\text{wFe}} = [(A_{\text{hm}} + B_{\text{m}}) (A_{\text{mw}} + B_{\text{w}} + B_{\text{Fe}} + F) + A_{\text{mw}} (B_{\text{w}} + B_{\text{Fe}} + F)] / W, \quad (13)$$

where

$$W = A_{\text{wFe}} (A_{\text{mw}} + B_{\text{w}} + B_{\text{Fe}} + F) + (A_{\text{mw}} + B_{\text{w}}) (B_{\text{Fe}} + F). \quad (14)$$

Thus, the total reaction rate of the gas can be expressed as $\dot{m}_j = \dot{m}_j^{\text{hm}} + \dot{m}_j^{\text{mw}} + \dot{m}_j^{\text{wFe}}$.

If the molar fraction of the reducing gas is lower than the equilibrium molar fraction of the gas in reaction $\text{w} \rightarrow \text{Fe}$ at a certain temperature, there may be six resistance networks as shown in Figure 2 (b~g) during the reaction. The reaction rate of reducing gas can be expressed as:

$$\dot{m}_j = \dot{m}_j^{\text{hm}} + \dot{m}_j^{\text{mw}} = \frac{\eta_j A_{pi}}{T_{pi}} \frac{M_j p_g}{R_g} \left[v_1 (x_j - x_{\text{eq},j}^{\text{hm}}) + v_2 (x_j - x_{\text{eq},j}^{\text{mw}}) \right]_j. \quad (15)$$

(i) When the molar fraction of the reducing gas is lower than the equilibrium molar fraction of the gas in reaction $\text{m} \rightarrow \text{w}$, only the reaction $\text{h} \rightarrow \text{m}$ occurs, and the product layer is only m (Figure 2 (b)). Thus, $v_1 = 1 / (A_{\text{hm}} + B_{\text{m}} + F)$ and $v_2 = 0$. (ii) When the molar fraction of the reducing gas is lower than the equilibrium molar fraction of the gas in reaction $\text{m} \rightarrow \text{w}$, only the reaction $\text{h} \rightarrow \text{m}$ occurs, and the product layers contain m and w (Figure 2 (c)). Thus, $v_1 = 1 / (A_{\text{hm}} + B_{\text{m}} + B_{\text{w}} + F)$ and $v_2 = 0$. (iii) When the molar fraction of the reducing gas is lower than the equilibrium molar fraction of the gas in reaction $\text{m} \rightarrow \text{w}$, only the reaction $\text{h} \rightarrow \text{m}$ occurs, and the product layer contains m and Fe (Figure 2 (d)). Thus, $v_1 = 1 / (A_{\text{hm}} + B_{\text{m}} + B_{\text{Fe}} + F)$ and $v_2 = 0$. (iv) When the molar fraction of the reducing gas is lower than the equilibrium molar fraction of the gas in reaction $\text{m} \rightarrow \text{w}$, only the reaction $\text{h} \rightarrow \text{m}$ occurs, and the product layer consists of m , w and Fe (Figure 2 (e)). Thus, $v_1 = 1 / (A_{\text{hm}} + B_{\text{m}} + B_{\text{w}} + B_{\text{Fe}} + F)$ and $v_2 = 0$. (v) When

Table 2: Hematite reduction by steps.

Reaction	k_0 [48]	E_a [48]	K_{eq} [47]
R1	29.17	66974	$\exp(1433.4/T_p + 9.08)$
R2	15.56	75345	$\exp(-7393.9/T_p + 7.56)$
R3	2858	117204	$\exp(-2023.8/T_p + 1.24)$

the molar fraction of the reducing gas is higher than the equilibrium molar fraction of the gas in reaction $m \rightarrow w$, but lower than that in reaction $w \rightarrow Fe$, both the reaction $h \rightarrow m$ and $m \rightarrow w$ occur, and the product layer consists of m and w (Figure 2 (f)). Thus, $v_1 = A_{mw}/W$ and $v_2 = (A_{hm} + B_m)/W$, where

$$W = A_{mw} (A_{hm} + B_m + B_w + F) + (A_{hm} + B_m) (B_w + F). \quad (16)$$

(vi) When the molar fraction of the reducing gas is higher than the equilibrium molar fraction of the gas in reaction $m \rightarrow w$, but lower than that in reaction $w \rightarrow Fe$, both the reaction $h \rightarrow m$ and $m \rightarrow w$ occur, and the product layer consists of m , w and Fe (Figure 2 (g)). Thus, $v_1 = A_{mw}/W$ and $v_2 = (A_{hm} + B_m)/W$, where

$$W = A_{mw} (A_{hm} + B_m + B_w + B_{Fe} + F) + (A_{hm} + B_m) (B_w + B_{Fe} + F). \quad (17)$$

The resistance at the reaction interface is:

$$A_{kl,j} = \left[\frac{1}{k_{r,kl}} (1 - f_k)^{-\frac{2}{3}} \frac{K_{eq,kl}}{1 + K_{eq,kl}} \right]_j, \quad (18)$$

$$k_r = k_0 \exp(-E_a/(R_g T_p)), \quad (19)$$

where k_r and k_0 is the reaction rate constant and pre-exponential factor respectively, and E_a is the activation energy. Kinetic parameters of each reaction are shown in Table 2.

Diffusion resistance of reducing gas j through product layer l is:

$$B_{l,j} = \left\{ \left[(1 - f_{l-1})^{-1/3} - (1 - f_l)^{-1/3} \right] \frac{r_p}{D_{eff}^l} \right\}_j, \quad (20)$$

where D_{eff}^l is the effective diffusion coefficient of gas through the product layer l . f_l is the fractional reduction degree, which can be calculated by the following equation [31]:

$$f_h = \frac{\frac{3m_m}{M_m} + \frac{m_w}{M_w} + \frac{m_{Fe}}{M_{Fe}}}{\frac{2m_h}{M_h} + \frac{3m_m}{M_m} + \frac{m_w}{M_w} + \frac{m_{Fe}}{M_{Fe}}}, \quad (21)$$

$$f_m = \frac{\frac{m_w}{M_w} + \frac{m_{Fe}}{M_{Fe}}}{\frac{2m_h}{M_h} + \frac{3m_m}{M_m} + \frac{m_w}{M_w} + \frac{m_{Fe}}{M_{Fe}}}, \quad (22)$$

$$f_w = \frac{\frac{m_{Fe}}{M_{Fe}}}{\frac{2m_h}{M_h} + \frac{3m_m}{M_m} + \frac{m_w}{M_w} + \frac{m_{Fe}}{M_{Fe}}}. \quad (23)$$

The overall reduction degree is:

$$f_{ov} = \frac{1}{9} f_h + \frac{2}{9} f_m + \frac{6}{9} f_w. \quad (24)$$

If magnetite is used as raw iron ore, the above equation becomes

$$f_{ov} = \frac{1}{4} f_m + \frac{3}{4} f_w. \quad (25)$$

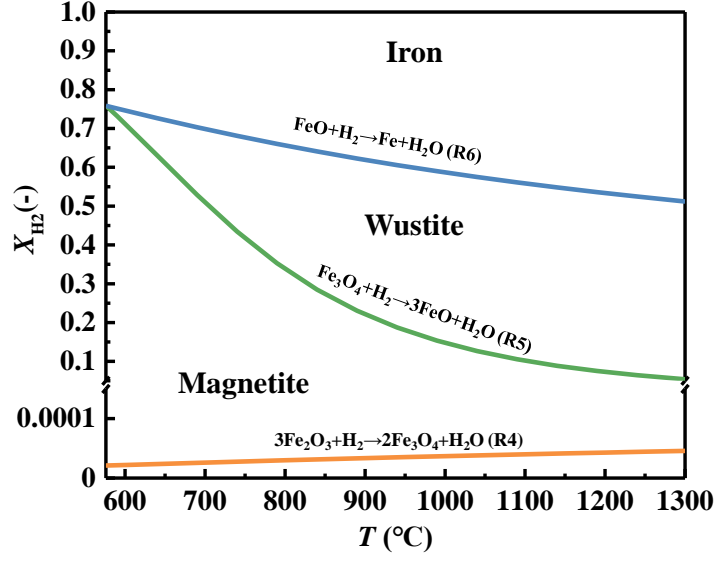


Figure 3: Thermodynamic equilibrium phase diagram of hematite reduced by H_2 , with the equilibrium constant cited from the fitting data of [47] ($T > 570^\circ C$).

Resistance of reducing agent through gas film is

$$F_j = \left(\frac{1}{\beta_f} \right)_j, \quad (26)$$

where β_f is the gas film mass transfer coefficient, which can be calculated as:

$$\beta_f = \frac{Sh D_{\text{eff},f}}{d_p}, \quad (27)$$

where the Sherwood number is [49]:

$$Sh = (7 - 10\varepsilon_g + 5\varepsilon_g^2)(1 + 0.7Re_p^{0.2}Sc^{1/3}) + (1.33 - 2.4\varepsilon_g + 1.2\varepsilon_g^2)Re_p^{0.7}Sc^{1/3}. \quad (28)$$

Particle Reynolds number and Schmidt number are respectively

$$Re_p = \frac{\rho_g \varepsilon_g d_p |\mathbf{u}_g - \mathbf{v}_p|}{\mu_g}, \quad (29)$$

$$Sc = \frac{\mu_g}{\rho_g D_{\text{eff},f}}, \quad (30)$$

where $D_{\text{eff},f}$ is the effective diffusion coefficient of reducing agent through the gas film, which is calculated by Equation 35. The mass change rate of the other component o in reaction $k \rightarrow l$ is expressed by the mass change rate of the reducing gas:

$$\dot{m}_o^{kl} = \frac{\eta_o^{kl} M_o}{\eta_j^{kl} M_j} \dot{m}_j^{kl}. \quad (31)$$

2.2. Reaction rate model: the raw iron ore is magnetite

According to the thermodynamic equilibrium phase diagram of hematite reduced by H_2 (Figure 3), if the raw iron ore consists of Fe_3O_4 and FeO , the reaction resistance network is shown as Figure 4. The reaction rate of reducing

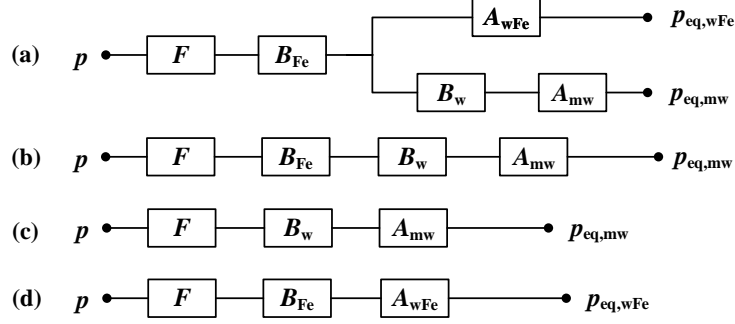


Figure 4: Resistance network for progressive reduction of magnetite.

gas can be expressed as:

$$\dot{m}_j = \dot{m}_j^{\text{mw}} + \dot{m}_j^{\text{wFe}} = \frac{\eta_j A_{pi}}{T_{pi}} \frac{M_j p_g}{R_g} \left[v_2 (x_j - x_{\text{eq},j}^{\text{mw}}) + v_3 (x_j - x_{\text{eq},j}^{\text{wFe}}) \right]_j. \quad (32)$$

(i) When the molar fraction of the reducing gas is higher than the equilibrium molar fraction of the gas in reaction $w \rightarrow \text{Fe}$, both the reaction $m \rightarrow w$ and $w \rightarrow \text{Fe}$ occur (Figure 4 (a)). Thus, $v_2 = A_{\text{wFe}}/W$, and $v_3 = (A_{\text{mw}} + B_w)/W$ in above equation, where

$$W = A_{\text{wFe}} (A_{\text{mw}} + B_w + B_{\text{Fe}} + F) + (A_{\text{mw}} + B_w) (B_{\text{Fe}} + F). \quad (33)$$

(ii) When the molar fraction of the reducing gas is lower than the equilibrium molar fraction of the gas in reaction $w \rightarrow \text{Fe}$, only the reaction $m \rightarrow w$ occurs (Figure 4 (b)). Thus, $v_2 = 1/(A_{\text{mw}} + B_w + B_{\text{Fe}} + F)$ and $v_3 = 0$. (iii) When the molar fraction of the reducing gas is lower than the equilibrium molar fraction of the gas in reaction $w \rightarrow \text{Fe}$, only the reaction $m \rightarrow w$ occurs, and the product layer does not contain Fe (Figure 4 (c)). Thus, $v_2 = 1/(A_{\text{mw}} + B_w + F)$ and $v_3 = 0$. (iv) When m has been completely converted to w, only the reaction $m \rightarrow w$ occurs (Figure 4 (d)). Thus, $v_2 = 0$, and $v_3 = 1/(A_{\text{wFe}} + B_{\text{Fe}} + F)$.

2.3. Gas diffusion in a porous particle

The diffusion of gas through porous solids depends on pore structure, porosity, tortuosity and pore size distribution. Gas diffusion within pores can be divided into two forms according to the relative magnitude of pore diameter (d_a) and the mean free path of molecular motion (λ). When $\lambda_j/d_a \leq 0.01$ ($\lambda_j = 1.013/(p_g x_j)$, cm), molecular diffusion is dominant [50], and the Fuller-Schettler-Giddings correlation [51] is used to calculate the bimolecular diffusion coefficient (unit: m^2/s):

$$D_{ij} = \frac{10^{-7} T_g^{1.75} (M_i^{-1} + M_j^{-1})^{1/2}}{(p_g/101325) (V_{d,i}^{1/3} + V_{d,j}^{1/3})^2}, \quad (34)$$

where M_i and M_j are expressed in g/mol, and $V_{d,i}$ and $V_{d,j}$ (cm^3/mol) are diffusion volume of gas i and j , respectively. In this study, $V_{d,\text{H}_2} = 7.07$, $V_{d,\text{H}_2\text{O}} = 12.7$ and $V_{d,\text{N}_2} = 17.9$. For a multi-component gas mixture, the molecular diffusion coefficient is [52]:

$$D_i^m = (1 - x_i) \left(\sum_{i \neq j} x_j / D_{ij} \right)^{-1}. \quad (35)$$

While $\lambda_j/d_a \geq 10$, diffusion inside the pore is called the Knudsen diffusion [50]. Most collisions occur between molecules and pore wall, and the collisions between molecules have little impact on the transport process. Therefore the Knudsen diffusion coefficient is determined by the pore radius, and not influenced by other gas species in the system. Its value can be calculated by

$$D_i^K = 0.97 r_a \sqrt{T_g/M_i}, \quad (36)$$

where r_a is pore radius (unit: cm). If the relative magnitude of λ and d_a lies between these two extreme cases, both molecular and Knudsen diffusions should be taken into account, and the total diffusion coefficient for species i is:

$$D_i = \frac{1}{1/D_i^m + 1/D_i^K}, \quad (37)$$

where the effective diffusion coefficient of gas i through product layer l is [53]

$$D_{\text{eff},i}^l = D_i \xi_l / \tau. \quad (38)$$

where τ is tortuosity. ξ_l is the porosity of l , its value varies with time and can be calculated based on the initial porosity of the particle. For porous particle, there is

$$\xi_l = 1 - \rho_{\text{eff},l} / \rho_{\text{true},l}, \quad (39)$$

where $\rho_{\text{eff},l}$ and $\rho_{\text{true},l}$ are the effective and true density of particle layer l , respectively. Assuming that the porosity of hematite core is equal to the porosity of the particle, the effective density of hematite core is:

$$\rho_{\text{eff},h} = (1 - \xi_p) \rho_{\text{true},h}. \quad (40)$$

The effective density of each product layer is respectively [37]

$$\rho_{\text{eff},m} = \rho_{\text{eff},h} q_{m,h}, \quad (41)$$

$$\rho_{\text{eff},w} = \rho_{\text{eff},m} q_{w,m}, \quad (42)$$

$$\rho_{\text{eff},\text{Fe}} = \rho_{\text{eff},w} q_{\text{Fe},w}, \quad (43)$$

where $q_{b,a}$ represents the equivalent mass of product b when the consumption of reactant a is 1, which can be calculated by [37]

$$q_{b,a} = \frac{|\eta_b| M_b}{|\eta_a| M_a}. \quad (44)$$

Accordingly, it is easy to calculate the values of $q_{m,h}$, $q_{w,m}$ and $q_{\text{Fe},w}$ as 0.9666, 0.9309 and 0.7773, respectively, and thus the porosity of each product layer was obtained by combining Equations 39, 41~43.

3. CFD-DEM method

3.1. Governing equations for particles

According to the conservation of particle mass, there are:

$$\dot{m}_p = \sum_z \dot{m}_z, \quad (45)$$

$$\dot{m}_z = \sum \dot{m}_z^{kl}, \quad (46)$$

where \dot{m}_p is the mass change rate of the particle, z represents the particle component Fe_2O_3 , Fe_3O_4 , FeO or Fe , and \dot{m}_z^{kl} is the mass change rate of z in the reaction $k \rightarrow l$, calculated by Equation 31.

The translational and rotational motion of particles can be described by the Newton's second law. The translational equation is written as:

$$\frac{d(m_p \mathbf{v}_p)}{dt} = \mathbf{F}_g + \mathbf{F}_p + \sum_{b=1}^{n_b} \mathbf{F}_{c,ab} + \mathbf{F}_{d,p} \quad (47)$$

$$m_p = m_0 + \dot{m}_p \Delta t_{\text{CFD}}, \quad (48)$$

where m_p and \mathbf{v}_p are the particle mass and velocity, respectively. m_0 is the particle mass of the previous CFD step, Δt_{CFD} is the time step of gas phase evolution. The gravity $\mathbf{F}_g = m_p \mathbf{g}$, and the pressure gradient force $\mathbf{F}_p = -V_p \nabla p_g$.

The contact force between particle a and b is expressed as $\mathbf{F}_{c,ab} = \mathbf{F}_{n,ab} + \mathbf{F}_{t,ab}$, where the details of normal contact force ($\mathbf{F}_{n,ab}$) and tangential contact force ($\mathbf{F}_{t,ab}$) can be seen in [54]. The gas-solid drag force is:

$$\mathbf{F}_{d,p} = \frac{\beta V_p}{1 - \varepsilon_g} (\mathbf{u}_g - \mathbf{v}_p) \quad (49)$$

where the drag coefficient β is calculated by Gidaspow's correlation [55], i.e.

$$\beta = \begin{cases} 150 \frac{\varepsilon_p^2 \mu_g}{\varepsilon_g d_p^2} + 1.75 \frac{\varepsilon_g \rho_g |\mathbf{u}_g - \mathbf{v}_p|}{d_p}, & \varepsilon_g < 0.8 \\ \frac{3}{4} C_D \frac{\varepsilon_p \varepsilon_g \rho_g |\mathbf{u}_g - \mathbf{v}_p|}{d_p} \varepsilon_g^{-2.65}, & \varepsilon_g > 0.8, \end{cases} \quad (50)$$

If the iron ore is non-spherical, the Gidaspow model is modified with the sphericity to obtain the Gidaspow-Ganser drag force correlation [56, 57], that is:

$$\beta = \begin{cases} 150 \frac{\varepsilon_p^2 \mu_g}{\varepsilon_g d_p^2 \psi^2} + 1.75 \frac{\varepsilon_g \rho_g |\mathbf{u}_g - \mathbf{v}_p|}{d_p \psi}, & \varepsilon_g < 0.8 \\ \frac{3}{4} C_D \frac{\varepsilon_p \varepsilon_g \rho_g |\mathbf{u}_g - \mathbf{v}_p|}{d_p} \varepsilon_g^{-2.65}, & \varepsilon_g > 0.8, \end{cases} \quad (51)$$

where ψ is the sphericity of the particle, and the drag coefficient of a single particle C_D is calculated by Ganser correlation [56]:

$$C_D = \frac{24}{Re_p K_1} \left[1.0 + 0.1118 (Re_p K_1 K_2)^{0.6567} \right] + \frac{0.4305 K_2}{1 + 3305 / (Re_p K_1 K_2)}, \quad (52)$$

$$K_1 = \left(\frac{1}{3} + \frac{2}{3} \psi^{-0.5} \right)^{-1} - 2.25 \frac{d_p}{D}, \quad (53)$$

$$K_2 = 10^{1.8148(-\log \psi)^{0.5743}}, \quad (54)$$

where D is the equivalent-area bed diameter. In addition, the momentum exchange caused by mass exchange is 0, so this term does not appear on the right side of Equation 47 according to the discussion of [58].

The particle rotation equation is [59]

$$\frac{d(\omega_p I_p)}{dt} = \mathbf{R}_p \times \mathbf{F}_t - \mu_r r_p |\mathbf{F}_n| \omega_p, \quad (55)$$

where

$$I_p = \frac{2}{5} m_p r_p^2, \quad (56)$$

where ω_p and I_p are the angular velocity and moment of inertia of the particle, respectively.

The particle energy conservation equation is

$$\frac{d(m_p C_{p,p} T_p)}{dt} = Q_{\text{conv}} + \sum_{b=1}^{n_b} Q_{ab} + Q_t + Q_{\text{rm}} + Q_{\text{pw}} + Q_{\text{rad}}, \quad (57)$$

$$C_{p,p} = \sum Y_z C_{p,z}, \quad (58)$$

where Y_z and $C_{p,z}$ are the mass fraction and heat capacity of particle component z respectively, and $C_{p,z}$ is a function of particle temperature, which can be calculated by Equation 74 and Table A1. The rate of heat flow due to gas convection is:

$$Q_{\text{conv}} = h_p A_p (T_g - T_p), \quad (59)$$

with

$$h_p = \frac{Nu \lambda_g}{d_p}, \quad (60)$$

where λ_g is the thermal conductivity coefficient of the gas phase, and Nu can be calculated by Gunn's empirical

correlation [49]:

$$Nu = (7 - 10\varepsilon_g + 5\varepsilon_g^2)(1 + 0.7Re_p^{0.2}Pr^{1/3}) + (1.33 - 2.4\varepsilon_g + 1.2\varepsilon_g^2)Re_p^{0.7}Pr^{1/3}, \quad (61)$$

with

$$Pr = \frac{C_{p,g}\mu_g}{\lambda_g}. \quad (62)$$

The contact heat transfer rate between the particle a and b is the sum of heat conduction rates of particle-particle and particle-fluid-particle, i.e. $Q_{ab} = Q_{ab}^{pp} + Q_{ab}^{pfp}$, where the particle-particle heat transfer rate is [60]:

$$Q_{ab}^{pp} = 4R_{c,ab}\lambda_{e,ab}(T_b - T_a), \quad (63)$$

and the particle-fluid-particle heat transfer rate is [61]:

$$Q_{ab}^{pfp} = 2\pi\lambda_g(T_b - T_a) \times \int_{R_{in}}^{R_{out}} \frac{R}{d_{ab} - \sqrt{R_a^2 - R^2} - \sqrt{R_b^2 - R^2}} dR. \quad (64)$$

The heat conduction rate between particle a and the wall is the sum of heat conduction rates of the particle-wall and particle-fluid-wall, that is, $Q_{aw} = Q_{aw}^{pw} + Q_{aw}^{pfw}$, where [60, 61]

$$Q_{aw}^{pw} = 4R_{c,aw}\lambda_{e,aw}(T_w - T_a), \quad (65)$$

$$Q_{aw}^{pfw} = 2\pi\lambda_g(T_w - T_a) \int_{r_{in,w}}^{r_{out,w}} \frac{r_w}{L_w} dr. \quad (66)$$

The physical meaning and calculation of each variable in Equation 63, 64, 65 and 66 can be found in [62]. The radiation heat flow rate of single particle from the environment is:

$$Q_{rad} = \sigma\eta_p A_p (T_{se,p}^4 - T_p^4), \quad (67)$$

where σ represents the Stefan-Boltzmann constant ($5.67 \times 10^{-8} \text{ W/m}^2\text{K}^4$), and η_p is the particle emissivity. $T_{se,p}$ is the average temperature of particles and fluid in a sphere with a volume of Ω around the particles, which is calculated as [63]:

$$T_{se,p} = \varepsilon_g T_{g,\Omega} + (1 - \varepsilon_g) \frac{1}{n_{p,\Omega}} \sum_{a=1}^{n_{p,\Omega}} T_{p,a}, \quad (68)$$

where ε_g , T_g , Ω and $n_{p,\Omega}$ are the gas volume fraction, gas temperature and number of particles in the domain Ω , respectively. The radius of the sphere domain is generally chosen as $1.5d_p$ [63]. The heat flow rate caused by reduction reaction is:

$$Q_r = \sum Q_r^{kl}, \quad (69)$$

$$Q_r^{kl} = - \sum_z H_z \dot{m}_z^{kl}. \quad (70)$$

The heat transfer rate caused by mass transfer is given by [64]

$$Q_{rm} = \sum Q_{rm}^{kl}, \quad (71)$$

$$Q_{rm}^{kl} = - \sum_j H_j \dot{m}_j^{kl}, \quad (72)$$

where the subscripts z and j represent the solid and gas species in the reaction $k \rightarrow l$, respectively. H is the standard

formation enthalpy, which is a polynomial function of temperature and can be written as [65]:

$$H = R_g(a_1T + 1/2a_2T^2 + 1/3a_3T^3 + 1/4a_4T^4 + 1/5a_5T^5 + a_6)/M, \quad (73)$$

where M is the molar mass of a species and the relationship between specific heat and temperature is as follows:

$$C_p = R_g(a_1 + a_2T + a_3T^2 + a_4T^3 + a_5T^4)/M. \quad (74)$$

The value of a_i is given in Table A1.

3.2. Governing equations for gases

In the CFD-DEM method, the gas phase is described by continuum model, and the mass conservation equation expressed by local average variable in a computational grid is:

$$\frac{\partial}{\partial t}(\varepsilon_g \rho_g) + \nabla \cdot (\varepsilon_g \rho_g \mathbf{u}_g) = \sum M_{m,j}, \quad (75)$$

where

$$M_{m,j} = \frac{1}{V_{\text{cell}}} \sum_{pi=1}^{n_{p,\text{cell}}} \dot{m}_{j,pi}, \quad (76)$$

where $M_{m,j}$ is the cell-averaged mass transfer rate of reactant or product gas j (H_2 or H_2O), and $n_{p,\text{cell}}$ the number of particles in a gas cell.

The momentum equation is written as:

$$\frac{\partial}{\partial t}(\varepsilon_g \rho_g \mathbf{u}_g) + \nabla \cdot (\varepsilon_g \rho_g \mathbf{u}_g \mathbf{u}_g) + \nabla \cdot (\varepsilon_g \rho_g \mathbf{u}'_g \mathbf{u}'_g) = -\varepsilon_g \nabla p + \nabla \cdot (\varepsilon_g \boldsymbol{\tau}_g) + \varepsilon_g \rho_g \mathbf{g} + \mathbf{M}_F, \quad (77)$$

where

$$\mathbf{M}_F = K_{gp}(\mathbf{u}_g - \mathbf{u}_p), \quad (78)$$

$$K_{gp} = -\frac{1}{V_{\text{cell}} |\mathbf{u}_g - \mathbf{u}_p|} \sum_{pi=1}^{n_{p,\text{cell}}} \frac{\beta V_{pi}}{1 - \varepsilon_g} |\mathbf{u}_g - \mathbf{v}_{pi}|. \quad (79)$$

The third term on the left side of Equation 77 arises due to the pseudo-turbulence, which is usually neglected in CFD-DEM simulations due to the lack of a suitable closure. However, recent PR-DNS (Particle-resolved direct numerical simulation) data show that gas-phase velocity fluctuations can contribute significantly, even in laminar gas-solid flows. Mehrabadi [66] provided a closure for the PTRS components using fixed-bed simulations which is also validated as an approximation to high stokes number freely evolving suspensions. \mathbf{u}'_g is the pseudo-turbulence fluctuation of velocity, and the component form of pseudo-turbulent Reynolds stress (PTRS) tensor $\mathbf{R} = \mathbf{u}'_g \mathbf{u}'_g$ can be expressed as [66]:

$$R_{ij} = 2k_g \left(b_{ij} + \frac{1}{3} \delta_{ij} \right), \quad (80)$$

where k_g is the gas phase pseudo-turbulent kinetic energy, which is modeled by

$$\frac{k_g}{E_g} = 2\varepsilon_p + 2.5\varepsilon_p \varepsilon_g^3 \exp(-\varepsilon_p Re_m^{1/2}), \quad (81)$$

$$E_g = \frac{1}{2} |\mathbf{u}_g - \mathbf{u}_p|^2, \quad (82)$$

where \mathbf{u}_p is the cell-averaged particle velocity, and the components of anisotropy tensor parallel to and perpendicular to the mean slip velocity are given by

$$b_{pa} = \frac{0.523}{1 + 0.305 \exp(-0.114 Re_m)} \exp \left[\frac{-3.511 \varepsilon_p}{1 + 1.801 \exp(-0.005 Re_m)} \right], \quad (83)$$

$$b_{pe} = -\frac{1}{2}b_{pa}, \quad (84)$$

where Re_m is the Reynolds number based on cell-averaged slip velocity and size of particles. The PTRS tensor \mathbf{R} is the diagonal tensor, whose off-diagonal elements are zero, i.e. $\mathbf{R} = \text{diag}(R_{pa}, R_{pe}, R_{pe})$. It should be noted that the orientation of the axis of the tensor \mathbf{R} is a local coordinate system with respect to the slip velocity, which needs to be converted to the global Cartesian coordinate system using Gram-Schmidt method [67]. The viscous stress in the gas phase on the right side of the Equation 77 is:

$$\boldsymbol{\tau}_g = \mu_g(\nabla \mathbf{u}_g + \nabla \mathbf{u}_g^T) - \frac{2}{3}\mu_g(\nabla \cdot \mathbf{u}_g)\mathbf{I}, \quad (85)$$

where \mathbf{I} is the unit tensor. K_{gp} in Equation 78 is the momentum transfer coefficient, and \mathbf{u}_p is the cell-averaged particle velocity. It is believed that the momentum exchange rate caused by the interphase mass transfer is 0, and the specific explanation can refer to a relevant literature [58].

The energy equation for gas phase is:

$$\frac{\partial}{\partial t}(\varepsilon_g \rho_g C_{p,g} T_g) + \nabla \cdot (\varepsilon_g \rho_g \mathbf{u}_g C_{p,g} T_g) + \nabla \cdot (\varepsilon_g \rho_g C_{p,g} \mathbf{u}'_g T'_g) = \nabla \cdot (\varepsilon_g \lambda_g \nabla T_g) + M_h + M_r + M_{r,m}. \quad (86)$$

The third term on the left side of the above equation arises due to pseudo-turbulence, where T'_g is the pseudo-turbulence fluctuation of temperature, and $\mathbf{R}_T = \mathbf{u}'_g T'_g$ is pseudo-turbulence heat flux (PTHF) tensor. Sun [68] used particle-resolved direct numerical simulation (PR-DNS) method to develop a closed correlation suitable for $0 < \varepsilon_p \leq 0.5$ and $1 \leq Re_m < 100$, where the PTHF component parallel to the mean slip velocity is written as:

$$\frac{\alpha_{pa}}{\alpha_g} = \frac{1.4Re_m(Re_m+1.4)Pr \exp(-0.002089Re_m) [\varepsilon_g(-5.11\varepsilon_p+10.1\varepsilon_p^2-10.85\varepsilon_p^3)+1-\exp(-10.96\varepsilon_p)]}{3\pi\varepsilon_g^2 Nu(1.17\varepsilon_p-0.2021\varepsilon_p^{1/2}+0.08568\varepsilon_p^{1/4}) [1-1.6\varepsilon_p\varepsilon_g-3\varepsilon_p\varepsilon_g^4 \exp(-Re_m^{0.4}\varepsilon_p)]}, \quad (87)$$

$$Nu = (-0.46 + 1.77\varepsilon_g + 0.69\varepsilon_g^2)\varepsilon_g^{-3} + (1.37 - 2.4\varepsilon_g + 1.2\varepsilon_g^2)Re_m^{0.7}Pr^{1/3}. \quad (88)$$

Where α_g is thermal diffusion coefficient of gas phase ($\alpha_g = \lambda_g/(\rho_g C_{p,g})$). The PTHF component perpendicular to the mean slip velocity is:

$$\alpha_{pe} = \left(\frac{R_{pe}}{R_{pa}}\right)\alpha_{pa} = \left(\frac{3b_{pe} + 1}{3b_{pa} + 1}\right)\alpha_{pa}. \quad (89)$$

The PTHF tensor $\mathbf{R}_T = \mathbf{u}'_g T'_g = -\boldsymbol{\alpha}_{PT} \cdot \nabla T_g$, where the diagonal tensor $\boldsymbol{\alpha}_{PT} = \text{diag}(\alpha_{pa}, \alpha_{pe}, \alpha_{pe})$. Like the PTRS tensor, the axis orientation of $\boldsymbol{\alpha}_{PT}$ is a local coordinate system with respect to the slip velocity, which needs to be converted to the global Cartesian coordinate system using Gram-Schmidt method. M_h and $M_{r,m}$ in Equation 86 are gas-particle convection heat transfer rate and heat transfer caused by mass transfer, respectively, which can be calculated by:

$$M_h + M_{r,m} = -\frac{1}{V_{\text{cell}}} \sum_{pi=1}^{n_{p,\text{cell}}} (Q_{\text{conv},pi} + Q_{\text{tm},pi}). \quad (90)$$

The heat generation rate due to chemical reaction is:

$$M_r = -\sum_j H_j M_{m,j}. \quad (91)$$

The gas radiation between particle and gas can be ignored due to low gas emissivity [69].

The species transport equation for gas species j

$$\frac{\partial}{\partial t}(\varepsilon_g \rho_g Y_j) + \nabla \cdot (\varepsilon_g \rho_g \mathbf{u}_g Y_j) = \nabla \cdot (\varepsilon_g \rho_g D_j \nabla Y_j) + \nabla \cdot (\varepsilon_g \rho_g \mathbf{D}_{PT} \cdot \nabla Y_j) + M_{m,j}, \quad (92)$$

where the first term on the right side of the equation represents the molecular diffusion, and the second term is the pseudo-turbulence diffusion term. Y_j the mass fraction of species j , and the molecular diffusion coefficient of j in gas phase can be obtained using Equation 35. \mathbf{D}_{PT} represents the pseudo-turbulence diffusion coefficient, whose value is

equal to the tensor α_{pT} [67].

3.3. Coarse-grained CFD-DEM method for reacting flow

The fluidized bed reactor used for iron ore reduction contains a large number of fine particles, and the complete conversion of iron ore to metallic iron generally takes several minutes to tens of minutes, which leads to the high time cost of simulating the complete conversion cycle of particles using traditional CFD-DEM method. In this study, we adopted a coarse-graining strategy based on EMMS-DPM (Energy Minimization Multi-Scale-Discrete Particle Method) [70]. In this method, a small number of coarse-grained particles (CGPs) can be used instead of real particles to simulate large-scale systems for a long time. Coarse-grained method has been widely used in simulating gas-solid flow and heat transfer [54, 70, 71, 72, 73], but it is less used in mass transfer and chemical reaction [74, 75, 76]. In present work, the coarse-grained method for heat transfer proposed in [73] was adopted, and the mass transfer and reaction model of CGPs were derived from it. Readers can refer to [70] for the details of the coarse-grained model of particle-particle interaction, particle-wall interaction and gas-particle interphase momentum transfer. It is assumed that the density of CGP is equal to the density of real particle in present study, that is, the mass of coarse particle is $m_{CGP} = k^3 m_p$, where m_p is the mass of real particle and k ($k = d_{CGP}/d_p$) is the coarse-graining ratio. However, in the original EMMS-DPM method, there are voids inside CGP particle, and the void fraction is set as the voidage at the minimum fluidization condition. More discussions about this specific point can be found in [72].

The convective heat transfer rate between gas and the CGP is:

$$Q_{conv,CGP} = k^3 Q_{conv}. \quad (93)$$

Lu [73] deduced the relationship between the heat conduction rate of real particles with size d_p and the heat conduction rate of CGPs with size d_{CGP} as follows:

$$Q_{ip}^{pp} = \frac{Q_{CGP}^{pp}}{k^{9/4}} \sqrt{\frac{f(e_p)}{f(e_{CGP})}}, \quad (94)$$

where Q_{CGP}^{pp} is calculated by using Equation 63, and the function of restitution coefficient is expressed as follows:

$$f(e) = e^{\frac{-\zeta}{\sqrt{1-\zeta^2} \cos \zeta}}, \quad (95)$$

$$\zeta = \frac{-\ln e}{\sqrt{\pi^2 + (\ln e)^2}}, \quad (96)$$

$$e_{CGP} = \sqrt{1 + k(e_p^2 - 1)}. \quad (97)$$

Then, the particle-particle heat conduction rate in the coarse-grained system can be written as:

$$Q_{CGP}^{pp'} = k^3 Q_{ip}^{pp} = k^{3/4} \sqrt{\frac{f(e_p)}{f(e_{CGP})}} Q_{CGP}^{pp}. \quad (98)$$

The relationship between the heat conduction rate of real particle-fluid-particle with size d_p and the heat conduction rate of coarse-grained particle-fluid-particle with size d_{CGP} as follows [73]:

$$Q_{ip}^{pfp} = Q_{CGP}^{pfp}/k, \quad (99)$$

where Q_{CGP}^{pfp} is calculated by using Equation 64. Therefore, the particle-fluid-particle heat conduction rate in the coarse-grained system can be written as:

$$Q_{CGP}^{pfp'} = k^3 Q_{ip}^{pfp} = k^2 Q_{CGP}^{pfp}. \quad (100)$$

Similar to the contact heat transfer between CGPs, the heat transfer rate between the CGP and wall can be calculated

by the following equations:

$$Q_{\text{CGP}}^{\text{pw}'} = k^{3/4} \sqrt{\frac{f(e_p)}{f(e_{\text{CGP}})}} Q_{\text{CGP}}^{\text{pw}}, \quad (101)$$

$$Q_{\text{CGP}}^{\text{p}f\text{w}'} = k^2 Q_{\text{CGP}}^{\text{p}f\text{w}}, \quad (102)$$

where $Q_{\text{CGP}}^{\text{pw}}$ and $Q_{\text{CGP}}^{\text{p}f\text{w}}$ are calculated by Equation 65 and 66, respectively. The heat generation rate due to chemical reaction for each CGP is

$$Q_{\text{r,CGP}} = k^3 Q_{\text{r}}. \quad (103)$$

The heat transfer rate caused by the interphase mass transfer for each CGP is

$$Q_{\text{rm,CGP}} = k^3 Q_{\text{rm}}. \quad (104)$$

The radiation heat flow rate of single CGP from the environment is

$$Q_{\text{rad,CGP}} = k^3 Q_{\text{rad}}. \quad (105)$$

The mass transfer rate between the reduction gas j and the CGP is

$$\dot{m}_{j,\text{CGP}} = k^3 \dot{m}_j. \quad (106)$$

3.4. Thermophysical properties of reacting gases

Gas under normal pressure and high temperature condition can be regarded as an ideal gas, and its density is described by the ideal gas equation of state:

$$\rho_g = \frac{M_g p_g}{R_g T_g}. \quad (107)$$

The relationship between the viscosity of gas component j and the temperature is as follows

$$\mu_{g,j} = a_1 + a_2 T_g + a_3 T_g^2. \quad (108)$$

The coefficient a_i is given in Table A2 (scatter data from the National Institute of Standards and Technology (<https://webbook.nist.gov/>) and the coefficient is obtained by polynomial fitting). The gas phase viscosity is the mass weighting of the viscosity of each species, i.e. [77]

$$\mu_g = \sum Y_j \mu_{g,j}. \quad (109)$$

The specific heat of gas species j can be calculated by Equation 74, and the correlation coefficients are given in Table A1. The specific heat of gas phase is the mass weighting of the specific heat of each species, i.e. [78]

$$C_{p,g} = \sum Y_j C_{p,j}. \quad (110)$$

The thermal conductivity of gas species j is related to temperature as follows

$$\lambda_{g,j} = a_1 + a_2 T_g + a_3 T_g^2 + a_4 T_g^3 + a_5 T_g^4. \quad (111)$$

The coefficient a_i is given in Table A3. The thermal conductivity of gas phase is the mass weighting of the thermal conductivity of each species, i.e. [77]

$$\lambda_g = \sum Y_j \lambda_{g,j}. \quad (112)$$

4. Numerical method and simulation setup

In our previous studies, the hydrodynamic, heat and mass transfer behavior as well as catalytic reactions in gas-solid reactors have been successfully simulated using the CFD-DEM-IBM method [58, 62, 79, 80, 81, 82, 83, 84].

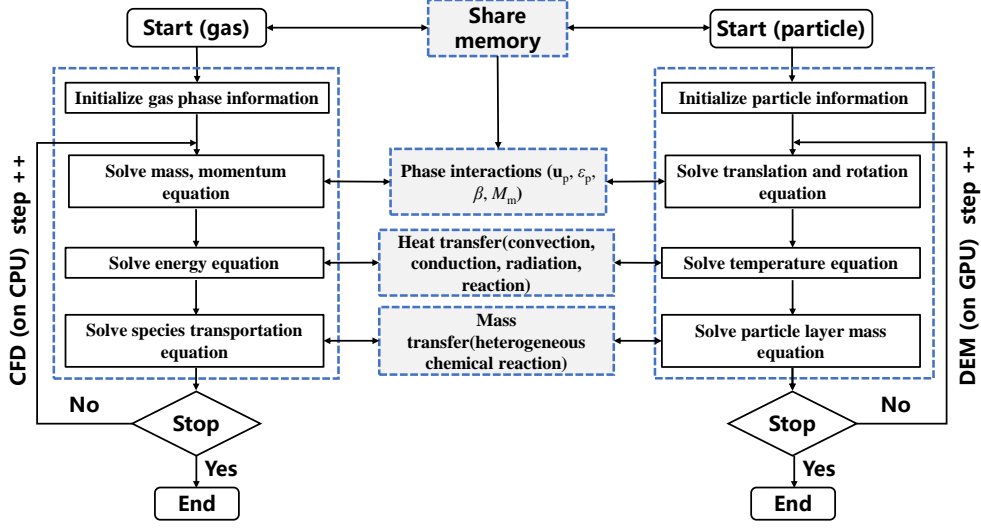


Figure 5: Flow chart of the CFD and DEM information exchange.

This study focuses on the implementation of the iron ore reduction reaction model on the CFD-DEM framework, so the details of IBM method are not given here again, which can be found in previous studies [62, 80]. The reduction reaction is accompanied by complex flow, mass and heat transfer, in which the gas and particles exchange information frequently. This is realized via sharing memory to establish a bridge of two-phase physical data communication. As shown in Figure 5, gas and particle information are obtained from the central processing unit (CPU) and graphics processing unit (GPU) respectively. The interaction information of the two phases is calculated on the GPU side and transmitted to the gas phase through shared memory. Meanwhile, the gas phase information in the grid is calculated at the CPU side and passed to the particle phase through the shared memory. It should be emphasized that the exchange of information between CFD and DEM does not take place at every step, but the coupling between CFD and DEM is completed every n ($n = \Delta t_{\text{CFD}}/\Delta t_{\text{DEM}}$) step. The solvers of gas and particles complete the evolution of each physical quantity in time and space through their respective iterative operations. The particle velocity and temperature are updated at each DEM step, while the mass of each product layer of the particle is updated only when the two phases are coupled.

In the CFD-DEM simulation of chemical reactions, large interphase source terms (momentum, heat, and mass) may cause instability or even divergence in the solution of gas phase fields (velocity, temperature, and species mass fraction), present study adopts the semi-implicit treatment of source terms to avoid this situation.

4.1. Semi-implicit treatment of source terms in momentum and energy equation

The momentum transfer source term in Equation 77 can be expressed as

$$\mathbf{M}_F = K_{gp}\mathbf{u}_g - K_{gp}\mathbf{u}_p. \quad (113)$$

Thus, the momentum equation is rewritten as

$$\frac{\partial}{\partial t}(\varepsilon_g\rho_g\mathbf{u}_g) + \nabla \cdot (\varepsilon_g\rho_g\mathbf{u}_g\mathbf{u}_g) + \nabla \cdot (\varepsilon_g\rho_g\mathbf{u}'_g\mathbf{u}'_g) - K_{gp}\mathbf{u}_g = -\varepsilon_g\nabla p + \nabla \cdot (\varepsilon_g\boldsymbol{\tau}_g) + \varepsilon_g\rho_g\mathbf{g} - K_{gp}\mathbf{u}_p, \quad (114)$$

where $K_{gp}\mathbf{u}_g$ and $K_{gp}\mathbf{u}_p$ are implicit and explicit source terms, respectively. When the temperature difference between gas and particle is high, it is necessary to transform the convection heat source term in the temperature Equation 86 as

follows

$$\begin{aligned}
M_h &= -\frac{1}{V_{\text{cell}}} \sum_{pi=1}^{n_{p,\text{cell}}} h_{pi} A_{pi} (T_g - T_{pi}) \\
&= -\frac{1}{V_{\text{cell}}} \left(T_g \sum_{pi=1}^{n_{p,\text{cell}}} h_{pi} A_{pi} - \sum_{pi=1}^{n_{p,\text{cell}}} h_{pi} A_{pi} T_{pi} \right) \\
&= -\frac{\sum_{pi=1}^{n_{p,\text{cell}}} h_{pi} A_{pi}}{V_{\text{cell}}} T_g + \frac{\sum_{pi=1}^{n_{p,\text{cell}}} h_{pi} A_{pi} T_{pi}}{V_{\text{cell}}} \\
&= -H_0 T_g + H_1,
\end{aligned}$$

where the coefficients H_0 and H_1 are respectively

$$H_0 = \frac{\sum_{pi=1}^{n_{p,\text{cell}}} h_{pi} A_{pi}}{V_{\text{cell}}}, \quad (115)$$

$$H_1 = \frac{\sum_{pi=1}^{n_{p,\text{cell}}} h_{pi} A_{pi} T_{pi}}{V_{\text{cell}}}. \quad (116)$$

In this way, the energy equation can be rewritten as

$$\frac{\partial}{\partial t} (\varepsilon_g \rho_g C_{p,g} T_g) + \nabla \cdot (\varepsilon_g \rho_g \mathbf{u}_g C_{p,g} T_g) + \nabla \cdot (\varepsilon_g \rho_g C_{p,g} \mathbf{u}'_g T'_g) + H_0 T_g = \nabla \cdot (\varepsilon_g \lambda_g \nabla T_g) + H_1 + M_r + M_{r,m}. \quad (117)$$

It should be noted that in the CFD simulation process, we found that the values of the reaction heat source term and the heat transfer source term caused by mass transfer are similar, and the sign is opposite, so the two terms remain explicit.

4.2. Semi-implicit treatment of mass source term in species transport equation

For reducing gas j , mass transfer rate on a single particle scale

$$\begin{aligned}
\dot{m}_{j,pi} &= \frac{\eta_j A_{pi}}{T_{pi}} \frac{M_j p_g}{R_g} \left[v_1 (x_j - x_{\text{eq},j}^{\text{hm}}) + v_2 (x_j - x_{\text{eq},j}^{\text{mw}}) + v_3 (x_j - x_{\text{eq},j}^{\text{wFe}}) \right]_j \\
&= \frac{\eta_j A_{pi}}{T_{pi}} \frac{M_j p_g}{R_g} \left[(v_1 + v_2 + v_3) x_j - (v_1 x_{\text{eq},j}^{\text{hm}} + v_2 x_{\text{eq},j}^{\text{mw}} + v_3 x_{\text{eq},j}^{\text{wFe}}) \right]_j,
\end{aligned} \quad (118)$$

where $v_1 = v_1^{\text{hm}} + v_1^{\text{mw}} + v_1^{\text{wFe}}$, $v_2 = v_2^{\text{hm}} + v_2^{\text{mw}} + v_2^{\text{wFe}}$, $v_3 = v_3^{\text{hm}} + v_3^{\text{mw}} + v_3^{\text{wFe}}$. Let $E_j = \eta_j A_{pi} / T_{pi}$, $Q_j = v_1 + v_2 + v_3$, $S_j = v_1 x_{\text{eq},j}^{\text{hm}} + v_2 x_{\text{eq},j}^{\text{mw}} + v_3 x_{\text{eq},j}^{\text{wFe}}$, then, we have

$$\begin{aligned}
\dot{m}_{j,pi} &= E_j M_j \left[Q_j x_j - S_j \right] \frac{p_g}{R_g} \\
&= E_j M_j Q_j x_j \frac{p_g}{R_g} - E_j S_j \frac{M_j}{R_g} p_g \\
&= E_j M_j Q_j \left(\frac{x'_j}{X_j} \right) \frac{p_g}{R_g} - E_j S_j \frac{M_j}{R_g} p_g \\
&= E_j M_j Q_j \left(\frac{M_g Y_j / M_j}{X_j} \right) \frac{p_g}{R_g} - E_j S_j \frac{M_j}{R_g} p_g \\
&= \frac{E_j Q_j \rho_g T_g}{X_j} Y_j - E_j S_j \frac{M_j}{R_g} p_g,
\end{aligned} \quad (119)$$

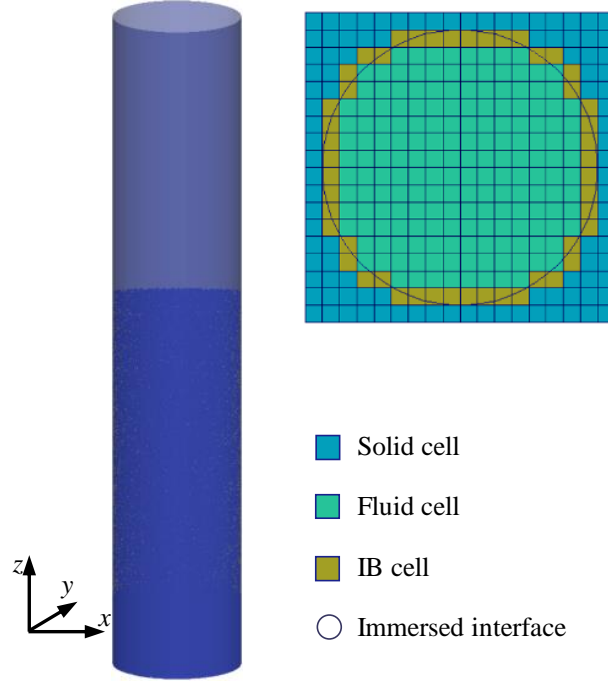


Figure 6: Schematic illustration of reduction reactor and grid distribution (top view).

where $X_j = x'_{\text{H}_2} + x'_{\text{H}_2\text{O}}$. By substituting Equations 119 and 76 into Equation 92, the species transport equation is rewritten as

$$\frac{\partial}{\partial t}(\varepsilon_g \rho_g Y_j) + \nabla \cdot (\varepsilon_g \rho_g \mathbf{u}_g Y_j) - C_0 \frac{\rho_g T_g}{X_j} Y_j = \nabla \cdot (\varepsilon_g \rho_g D_j \nabla Y_j) + \nabla \cdot (\varepsilon_g \rho_g \mathbf{D}_{\text{PT}} \cdot \nabla Y_j) + C_1 p_g. \quad (120)$$

Where C_0 and C_1 are respectively

$$C_0 = \frac{\sum_{p_i=1}^{n_{p,\text{cell}}} E_j Q_j}{V_{\text{cell}}}, \quad (121)$$

$$C_1 = -\frac{M_j}{R_g} \frac{\sum_{p_i=1}^{n_{p,\text{cell}}} E_j S_j}{V_{\text{cell}}}. \quad (122)$$

4.3. Simulation parameters and settings

In order to verify the correctness of the CFD-DEM-IBM method coupled with the USCM model, the reduction processes of magnetite and hematite were respectively simulated and compared with the experimental results of [18] and [20]. Magnetite is reduced in a bubbling fluidized bed with an inner diameter of 20 mm and a height of 60 mm, and the hematite reduction reactor has an inner diameter of 68 mm and a height of 200 mm. Figure 6 shows the schematic illustration of the reactor and the fluid grid distribution. Table 3 lists the simulation parameters and physical properties of the particle and gases. It should be pointed out that the magnetite and hematite particles used in the experiment both are irregular, so Equation 51 are used to calculate the drag coefficient. In addition, the discrete scheme of each term in the gas conservation equation are shown in Table 4.

Table 3: Parameters and physical properties used in present simulations.

	Parameter	Bed I	Bed II
Particle	Iron ore type	magnetite	hematite
	Initial efficient density, ρ_{p0} (kg/m ³)	3720	3500
	True density, ρ_{true} (kg/m ³)	5300(Fe ₂ O ₃), 5180(Fe ₃ O ₄), 5390(FeO), 7900(Fe)	
	Mean diameter of real particle, d_p (mm)	0.1	0.35
	Number of real particle	5140800	5095837
	Coarse-graining ratio, k	2.8	3.0
	Young's modulus, Y_p (Pa)		1×10^7
	Restitution coefficient of real particle, e_p		0.9
	Sliding friction coefficient, μ_s		0.3
	Rolling friction coefficient, μ_r (mm)		0.01
	Poisson's ratio, ν_p		0.3
	Characteristic velocity, u_c (m/s)		1.0
	Initial temperature, T_{p0} (K)	943, 923, 903	1073, 973
	Initial mass fraction (wt%)	69.94(Fe ₃ O ₄), 30.06(FeO)	96.28(Fe ₂ O ₃), 3.72(FeO)
	Initial porosity, ξ_0	0.29	0.34
	Pore diameter (cm), d_a	9.5×10^{-6}	3.3×10^{-6}
	Emissivity, η_p		0.85
	Sphericity, ψ	0.85	0.86
	Time step, Δt_{DEM} (s)	5×10^{-6}	2×10^{-5}
	Gas	Inlet composition, x_{j0} (vol%)	70(H ₂), 30(N ₂)
Inlet velocity, u_{g0} (m/s)		0.183, 0.179, 0.175	0.43, 0.39
Inlet temperature, T_{g0} (K)		943, 923, 903	1073, 973
Operating pressure, p_{g0} (Pa)		101325	110000
Grid size, $L_x \times L_y \times L_z$ (mm)		$1.25 \times 1.25 \times 1.25$	$4.25 \times 4.25 \times 4.25$
Time step, Δt_{CFD} (s)		1×10^{-4}	2×10^{-4}
Wall velocity			No slip
Boundary condition	Wall temperature (K)	943, 923, 903	1073, 973
	Outlet Pressure (Pa)	101325	110000

Table 4: Numerical scheme used in OpenFOAM.

Term	Discrete scheme
Time derivative	Euler
Temperature gradient	Gauss linear
Velocity gradient	CellLimited Gauss linear 1
Pressure gradient	Gauss linear
Convection (velocity)	GausslimitedLinearV 1
Convection (temperature)	Gauss upwind
Convection (species mass fraction)	limitedLinear01 1
Laplacian	Gauss linear corrected

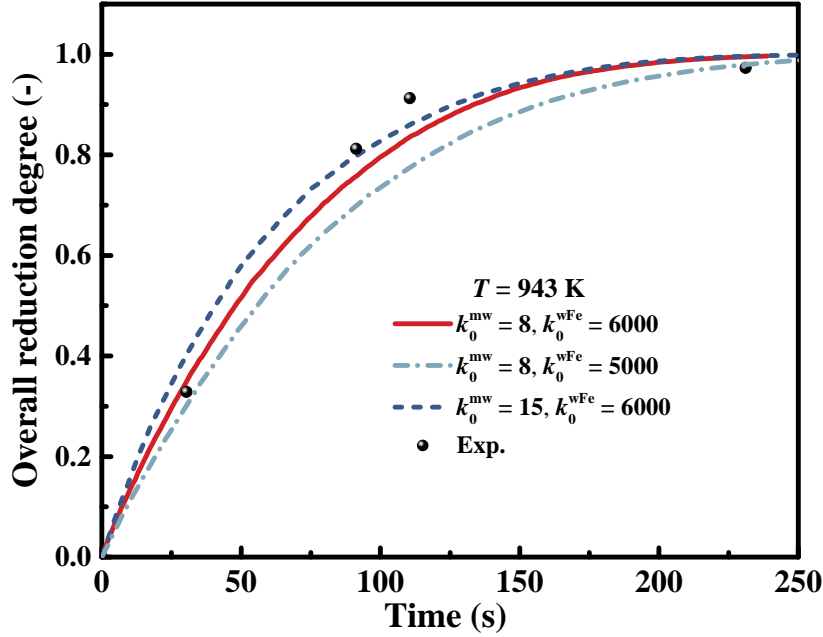


Figure 7: Effect of pre-exponential factors on magnetite reduction.

5. Results and discussion

5.1. Reduction of magnetite

5.1.1. Determination of reaction kinetic parameters and their influence

Reaction kinetic parameters (pre-exponential factor and activation energy) are crucial to the reduction reaction rate and iron ore conversion rate, which are generally determined by linear regression method in experiments [85, 20, 21]. Du [18] obtained the apparent activation energy of magnetite reduction in H_2 atmosphere by linear regression in the experiment, but the activation energy of each specific reaction was unknown, we adopted the values given in [48] for the activation energy of reaction R2 and R3 in CFD simulations: $E_a^{mw}=75345$ J/mol, $E_a^{wFe}=117204$ J/mol. Furthermore, the method provided by [48] was used to estimate the pre-exponential factor: values considered appropriate were substituted initially, and the pre-exponential factor was constantly adjusted on the premise of keeping other operating conditions unchanged, while the change in the reduction degree of the particles was monitored. When the reduction degree is in good agreement with the experimental results, the pre-exponential factor of each sub-reaction can be determined.

As shown in Figure 7, when the initial values of the pre-exponential factors of the reaction from Fe_3O_4 to FeO and FeO to Fe are 8 and 5000, respectively, the predicted overall reduction degree of magnetite deviates greatly from the experimental values, especially in the middle stages of the reaction. Therefore, by adjusting these two values, a set of pre-exponential factors that best agree with the experimental values are obtained successfully: $k_0^{mw}=8$ m/s, $k_0^{wFe}=6000$ m/s. The slope of the reduction curve represents the reaction rate. Before about 20 s, the particles undergo a constant rate transformation period. With the reduction of magnetite, the slope becomes smaller and the reaction rate slows down, indicating that the reaction resistance in the early stage is less than that in the later stage. Additionally, as the pre-exponential factor increases, the reaction rate constant increases, meaning that less time is required for the complete conversion of magnetite to metallic iron.

Figure 8 illustrates the effect of pre-exponential factors on the reduction degree of Fe_3O_4 (a) and FeO (b). It is obvious that the pre-exponential factor of the reaction $Fe_3O_4 \rightarrow FeO$ (k_0^{mw}) has a great influence on the reduction of $Fe_3O_4 \rightarrow FeO$, while the pre-exponential factor of the reaction $FeO \rightarrow Fe$ (k_0^{wFe}) has almost no effect on the conversion of Fe_3O_4 . It can be seen from Figure 8 (b) that at the initial stage of the reaction, the reduction degree of FeO depends

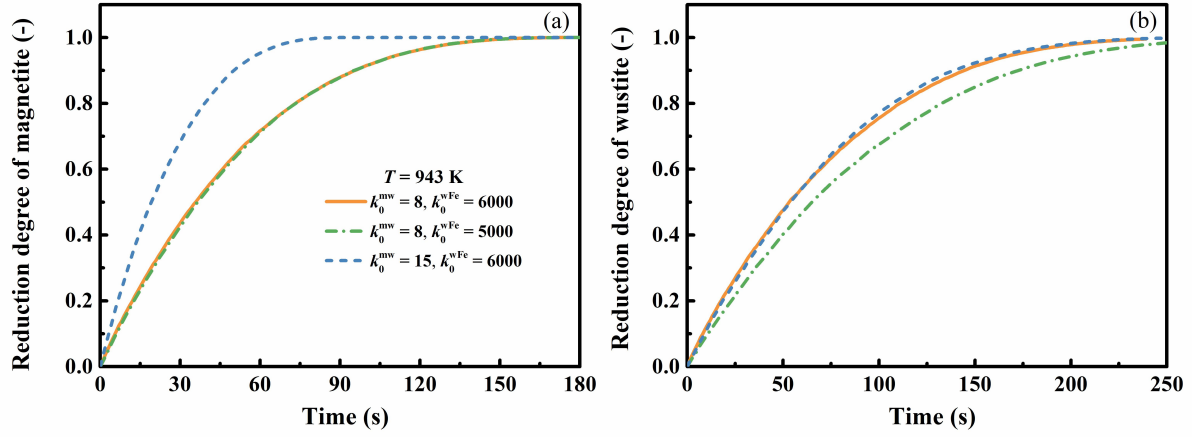


Figure 8: Effect of pre-exponential factors on fractional reduction.

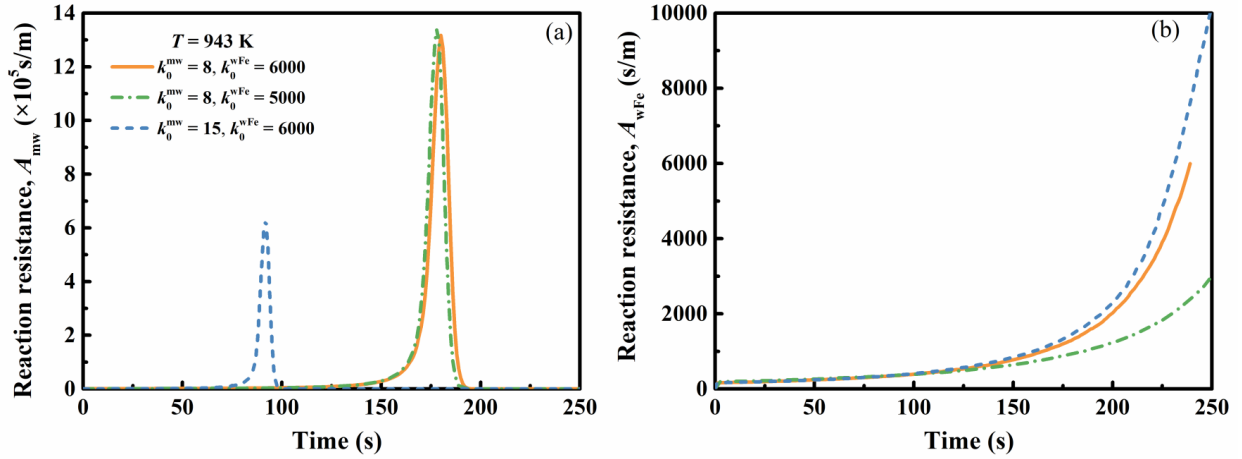


Figure 9: Effect of pre-exponential factors on the interfacial reaction resistance.

only on k_0^{wFe} , and has almost no relationship with k_0^{mw} . With the progress of the reaction, the increase of k_0^{mw} will slightly accelerate the conversion of FeO. The possible reason is that when k_0^{mw} changes from 8 to 15 (m/s), the time for the complete conversion of Fe_3O_4 to FeO is greatly shortened, and more hydrogen will react with FeO in the middle and late stage of the reaction, thus accelerating the reduction of FeO.

In Figure 9, the influence of pre-exponential factors on the interfacial reaction resistance is illustrated. As the reaction progresses, the chemical reaction resistance increases. As can be seen from Figure 9 (a), when Fe_3O_4 is almost completely converted into FeO, the interfacial reaction resistance of reaction from Fe_3O_4 to FeO (A_{mw}) reaches its peak value and then rapidly drops to zero, a similar phenomenon that was also observed by Kinaci[37]. At this time, Fe_3O_4 in the particle has been completely consumed, and the FeO formation reaction no longer occurs. According to Equation 18, when the reaction temperature changes within a narrow range, the reaction rate constant and reduction degree are the most critical variables affecting the interface reaction resistance. For a given reaction rate constant, the reaction resistance increases with the increase of the reduction degree, and when the reduction degree of the particles is the same (for example, the reduction degree of Fe_3O_4 corresponding to the peak value in Figure 8 (a) is about 1), the reaction rate constant is negatively correlated with the reaction resistance. Consistent with the change in reduction degree, A_{mw} is only related to A_{mw} , while A_{wFe} is not only closely related to k_0^{wFe} , but is also influenced by k_0^{mw} , for possible reasons already given in the discussion about Figure 8.

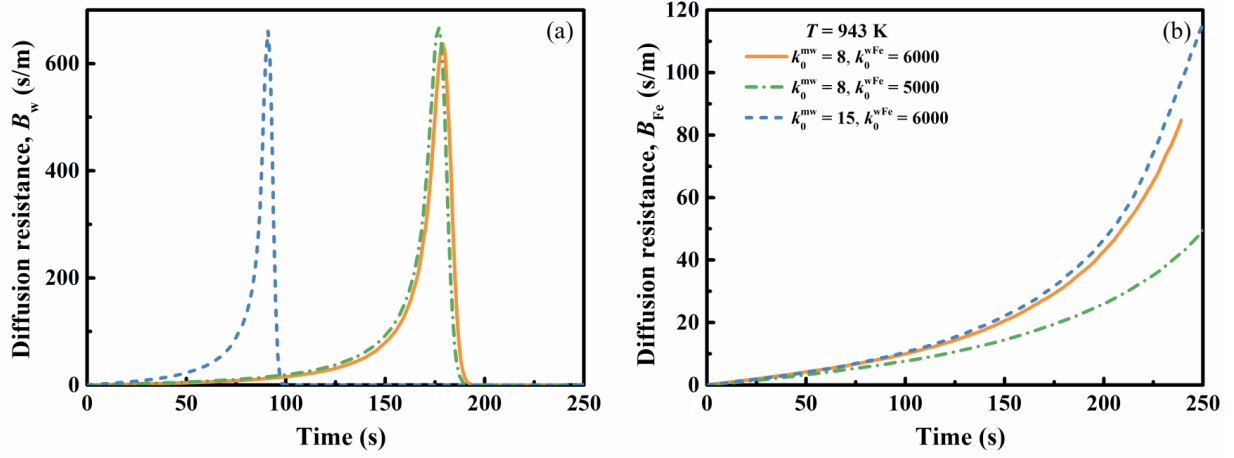


Figure 10: Effect of pre-exponential factors on the product layers diffusion resistance.

The influence of pre-exponential factors on the diffusion resistance of gas through the product layer is shown in Figure 10. With the reduction of magnetite, the thickness of the product layer increases, and its resistance to gas diffusion increases gradually. When Fe_3O_4 is completely reduced to FeO , the resistance (B_w) of the gas through the wustite reaches its peak. After this, B_w becomes 0 because there is only one product layer of metallic iron in the particle. The resistance of the gas through the iron layer (B_{Fe}) increases until the FeO is completely consumed. The variation trend of internal diffusion resistance with the pre-exponential factor is similar to that of the reaction resistance in Figure 10, and the analysis will not be carried out here.

As shown in Figure 11, in the magnetite reduction process, the mass transfer resistance through gas film fluctuates around an mean value ($F_{\text{mean}}=0.048$ s/m), and the pre-exponential factor has little influence on it. From Equations 26 and 27, it can be seen that the external diffusion resistance is only related to the diffusion coefficient $D_{\text{eff},f}$ and the dimensionless Sherwood number Sh of the reducing gas in the gas film, while the pre-exponential factor has little impact on these two gas-related variables. Therefore, the time-averaged value of the gas film resistance predicted by the three different pre-exponential factors is basically equal.

In summary, the interfacial reaction resistance is largest, and the order of each resistance is: $A_{\text{mw}} > A_{\text{wFe}} > B_w > B_{\text{Fe}} > F$. In other words, the chemical reaction at the interfaces is the dominant control mechanism during magnetite reduction. Most researchers [86, 29, 85] believe that a dense iron shell forms on the outer surface of the particle when wustite is reduced to metallic iron, and the diffusion of hydrogen through this shell becomes difficult, which is consistent with our findings.

5.1.2. Effect of temperature on magnetite reduction

Figure 12 shows the comparison of the reduction progress at different operating temperatures. The agreement between the measured and calculated values is very good at 943, 923, and 903 K, while the overall reduction degree at the final stage is less satisfactorily simulated (all overestimated). The possible reason is that our model does not take into account that the adhesion of iron to the surface of the wustite causes the reduction rate to be greatly reduced. Obviously, due to the heat absorption during magnetite reduction, the increase of operating temperature will accelerate the reaction rate, and the reduction degree and porosity of the particles will increase accordingly, but the final porosity does not change, about 0.55.

5.2. Reduction of hematite

5.2.1. Determination of reaction kinetic parameters and model validation

Spreitzer [87] obtained the activation energies of reactions $\text{Fe}_2\text{O}_3 \rightarrow \text{Fe}_3\text{O}_4$, $\text{Fe}_3\text{O}_4 \rightarrow \text{FeO}$ and $\text{FeO} \rightarrow \text{Fe}$ by fitting experimental data, which were 42.4, 19.3 and 33.88 (kJ/mol), respectively. When the operating temperature is 1073 K, the method in Section 5.1.1 is still used to estimate the pre-exponential factors of each sub-reaction, and the final

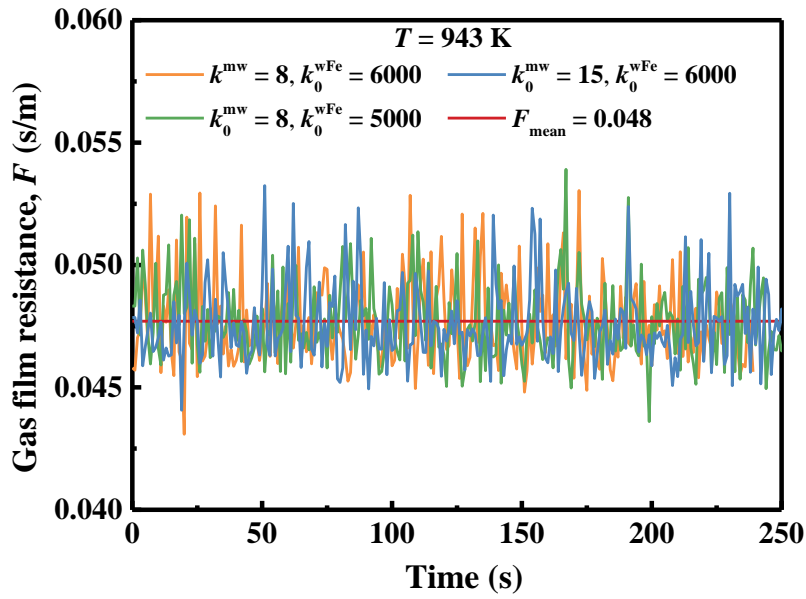


Figure 11: Effect of pre-exponential factors on gas film diffusion resistance.

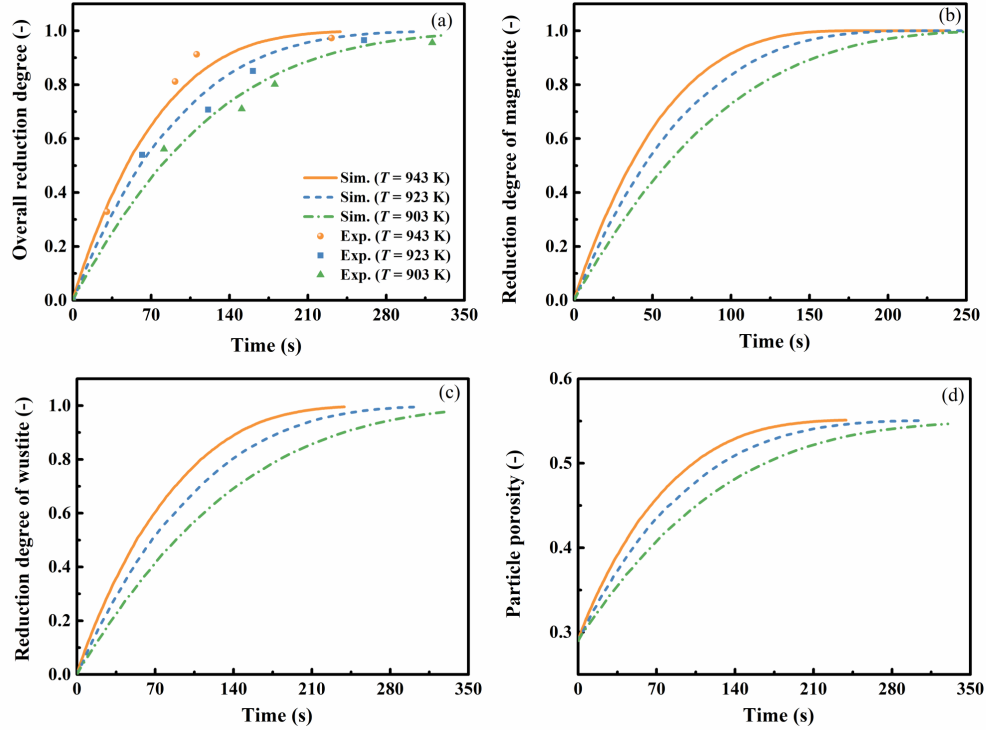


Figure 12: Effect of operating temperature on magnetite reduction.

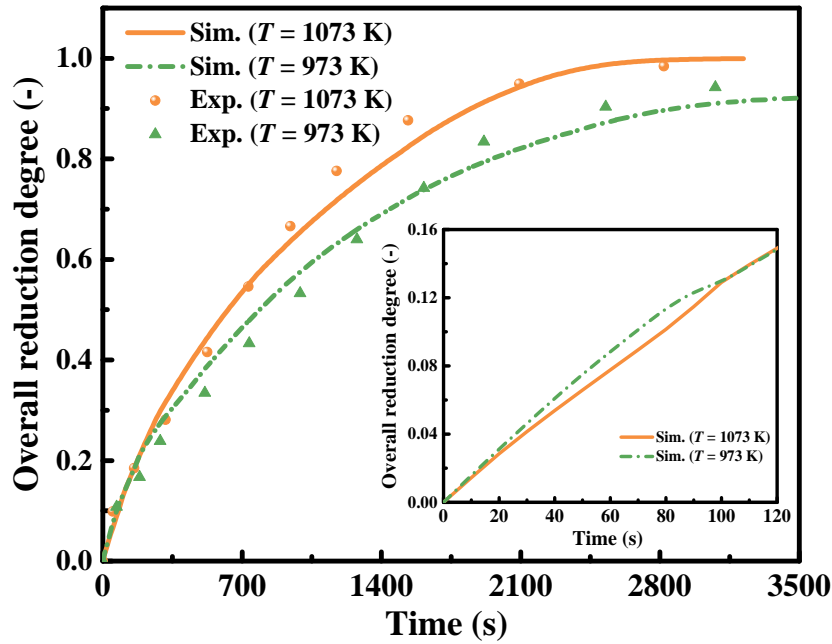


Figure 13: Effect of pre-exponential factors on hematite reduction.

pre-exponential factors are 10, 0.0007, 0.022 (m/s), respectively. Figure 13 shows the change of the overall reduction degree of hematite particles with time at 973 K, 1023 K and 1073 K. It can be seen that in a certain temperature range (973 K~1073 K), our model can accurately predict the direct reduction process of hematite in the mixed atmosphere of hydrogen and nitrogen. Hematite takes about an hour to be almost completely converted into metallic iron, while magnetite (Figure 5) takes less than five minutes. The reasons for this difference may be: (i) the average particle size of hematite is larger than that of magnetite, and (ii) the reaction rate constant of hematite is smaller than that of magnetite. The second reason may be dominant, and the effect of particle size on the reaction rate is actually small [18]. In the reaction from Fe_2O_3 to Fe_3O_4 , the equilibrium concentration of hydrogen is close to zero. In the initial stage ($t < 100$ s), most of the hydrogen is used to reduce Fe_2O_3 , and the generation of Fe_3O_4 is an exothermic process, so the reduction degree increases with the drop of temperature during this period (local zoom in Figure 13). After Fe_2O_3 is consumed, endothermic reaction occurs, and the increase in temperature is conducive to the reduction of particles. Similarly, the reduction rate is slower due to the deposition of iron on the particle surface.

In the reduction process of hematite, metallic iron is constantly generated, and the change of the rate of iron generation in each particle over time is shown in Figure 14. It can be seen that the rate of iron formation in the lower part of the bed is higher than that in the upper part. At the beginning of the reaction, only the conversion of Fe_2O_3 to Fe_3O_4 occurs in most of the particles in the bed, and no iron is formed. After 100 s, more and more particles complete the transition from hematite to metallic iron. Until 2000 s, a small number of particles were not completely reduced. Obviously, with the progress of the reaction, the expansion height of the bed increases, and the flow regime undergoes a transition from a fixed bed to a bubbling bed. This is because the particles become lighter when they are reduced, and the resultant force of the drag and gravity on the particles increases when the operating gas velocity is unchanged. Therefore, when hematite is completely reduced to Fe, the particles will be more easily carried by bubbles to the surface of the bed.

5.2.2. Effect of temperature on hematite reduction

Figure 15 gives the quantitative comparison among the changes of fractional reduction degree and particle porosity during hematite reduction at different operating temperatures. Obviously, because the reduction of Fe_2O_3 to Fe_3O_4 is an endothermic reaction, the reaction rate of Fe_2O_3 at higher temperatures is slower, which means a low fractional

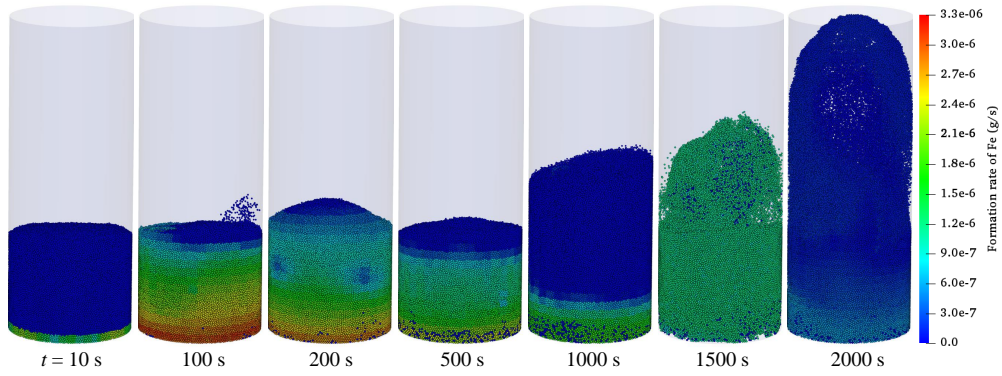


Figure 14: Evolution of iron formation rate at 1073 K.

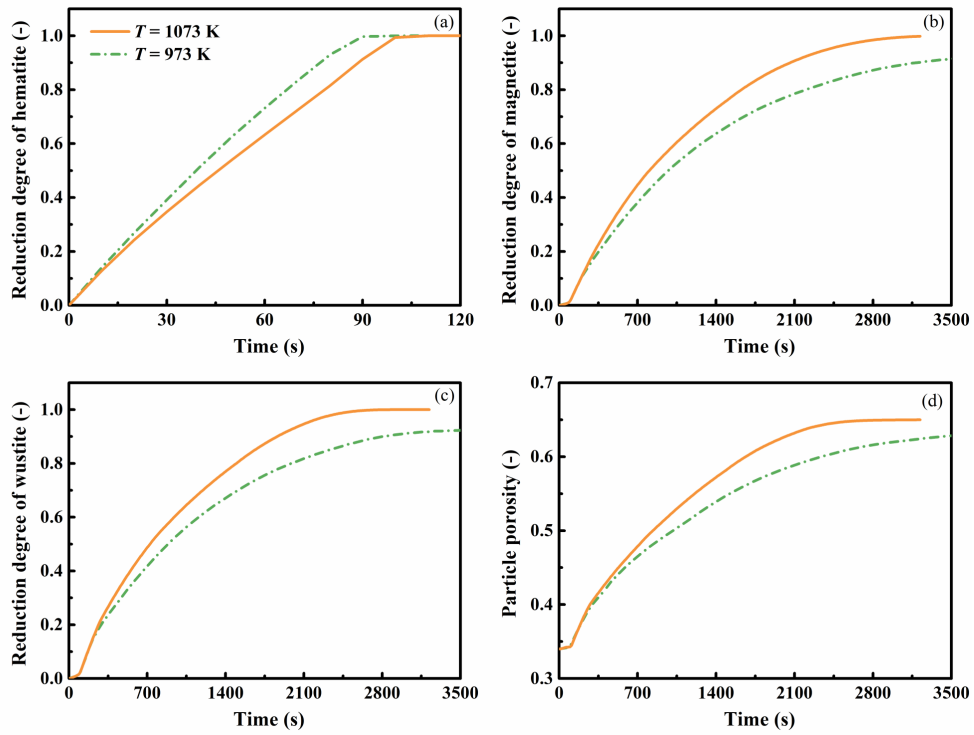


Figure 15: Effect of temperature on reduction degree and porosity.

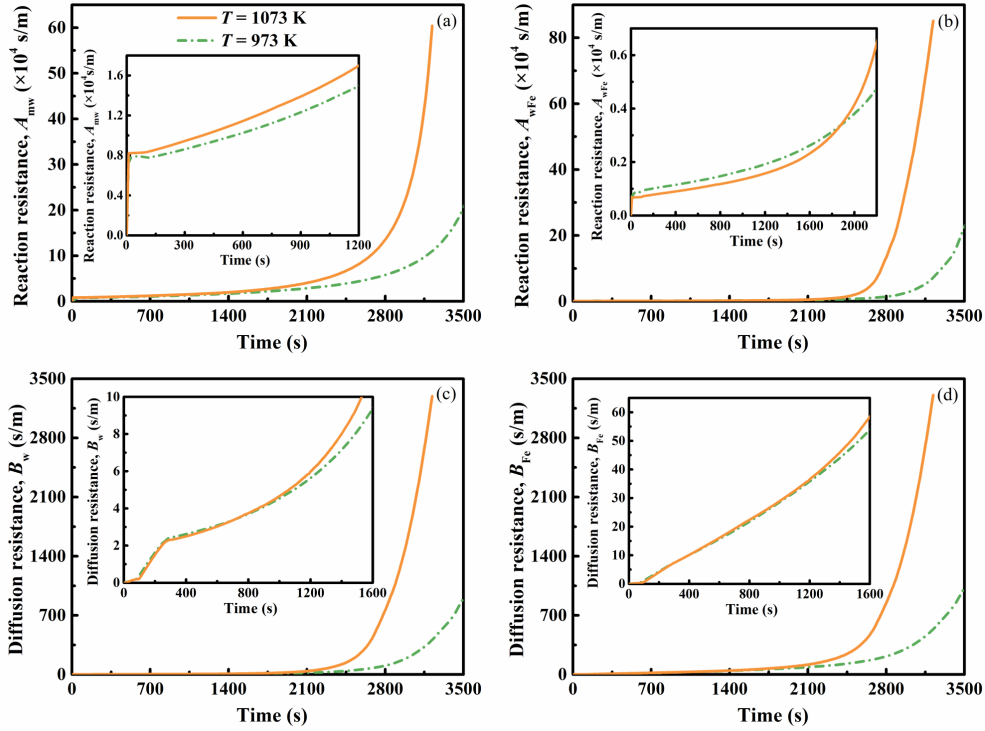


Figure 16: Effect of temperature on reaction resistance and diffusion resistance.

reduction. Before 100 s, the R1 reaction mainly occurs in the particle, so the reduction degree of Fe_3O_4 and FeO is very low. Furthermore, less reduction in particle mass at this stage leads to little change in porosity. After Fe_2O_3 is completely consumed, the reduction degree of Fe_3O_4 and FeO increases with the rise of temperature. When the operating temperature is 1073 K, the complete conversion of hematite to metallic iron takes about 3200 s, while at 973 K, the entire conversion process takes longer. The increase in the operating temperature accelerates the loss of oxygen and causes the porosity of the particles to increase until the end of the reaction, at which point the porosity is about 0.65. Overall, the high temperature is conducive to the reduction of iron ore with hydrogen.

Figure 16 shows the influence of temperature on interfacial chemical reaction resistance and gas diffusion resistance through the product layers during hematite reduction. With the progress of the reaction, both kinds of resistance increased, and the resistance increased sharply at the end of the reaction, which was consistent with the trend of resistance change of magnetite particles in Section 5.1. The influence trend of temperature on each resistance in the early stage of reaction is inconsistent (local enlarged figure), but the interface reaction resistance and internal diffusion resistance increase with the rise of temperature in the later stage. It can be explained by the following analysis: From Equation 18 and 19, it can be seen that heating increases the reaction rate constant, the reduction degree of Fe_3O_4 and FeO , and the equilibrium constant. The positive correlation between A_{mw} and temperature indicates that the reduction degree and equilibrium constant of Fe_3O_4 play a decisive role in the change of A_{mw} . The temperature at the early stage of the reaction has an inhibitory effect on A_{wFe} , indicating that the reaction rate constant is the main factor affecting A_{wFe} . At the later stage of the reaction, the increase of reduction degree became the dominant factor for the increase of resistance. In Figure 16 (c) and (d), the influence of temperature on diffusion resistance is similar to that of interface reaction resistance, which can be analyzed by Equation 20 and will not be repeated here. In addition, the time-averaged value of gas film diffusion resistance at 1073 K and 973 K are 0.14 and 0.12 (s/m), respectively. Therefore, the reduction of the hematite particles is also controlled by the interfacial chemical reaction, just like magnetite powder in Section 5.1.

6. Conclusion

The direct reduction of iron ore in hydrogen was simulated by using CPU-GPU hybrid parallel coarse-grained CFD-DEM-IBM method. Based on the USCM particle reaction model, a variety of resistance networks are considered in the modeling to reflect the real single particle reaction process. The kinetic parameters (pre-exponential factor) of each sub-reaction are determined by comparing the simulated and experimental values of the particle overall reduction. Heat transfer, mass transfer and chemical reaction behavior of magnetite and hematite particles in fluidized beds at high temperature were predicted. The following conclusions were drawn: (i) The CFD-DEM method coupled with USCM model can accurately predict the step-by-step reduction process of iron ore particles at high temperature; (ii) The interfacial chemical reaction of hematite and magnetite particles used in the simulation during reduction is a rate control step, and the interfacial reaction resistance > diffusion resistance of gas through product layer > gas film resistance, so appropriate reaction kinetic parameters is the key to accurately predict iron ore reduction; (iii) Heat is released when hematite is reduced to magnetite in hydrogen, and high temperature will inhibit the generation of magnetite, while the reduction of magnetite is an endothermic process, and rising temperature is conducive to the generation of iron; (iv) The complete conversion time of fine magnetite powder is much less than that of medium sized hematite particles. Clearly, the present work provides a computational tool for the rapid and efficient simulation of iron ore reduction in fluidized beds by combining the particle scale reaction model with the traditional CFD-DEM method, and reveals the reaction control mechanism and the basic principles of momentum, mass and energy transfer during fluidization reduction. It can be applied to the optimization and design of industrial reactors with complex geometric structures and large particle numbers, not only in fluidized beds, but also in metallurgical equipment such as blast furnaces.

CRedit authorship contribution statement

Bin Lan: Methodology, Software, Formal analysis, Investigation, Writing - original draft. **Ji Xu:** Software, Writing - review & editing. **Shuai Lu:** Formal analysis, Writing - review & editing. **Yige Liu:** Software, Writing - review & editing. **Fan Xu:** Formal analysis, Writing - review & editing. **Bidan Zhao:** Funding acquisition, Writing - review & editing. **Zheng Zou:** Funding acquisition, Writing - review & editing. **Ming Zhai:** Supervision, Writing - review & editing. **Junwu Wang:** Methodology, Conceptualization, Funding acquisition, Supervision, Writing - review & editing.

Declaration of Competing Interest

The authors declare that they have no known competing financial interests or personal relationships that could have appeared to influence the work reported in this paper.

Acknowledgement

This study is financially supported by the Strategic Priority Research Program of the Chinese Academy of Sciences (XDA29040200), the National Natural Science Foundation of China (21978295, 22311530057, 11988102), the Innovation Academy for Green Manufacture, Chinese Academy of Sciences (IAGM2022D02), the National Key R&D Program of China (2021YFB1715500), the Young Elite Scientists Sponsorship Program by CAST (2022QNRC001) and the Youth Innovation Promotion Association, Chinese Academy of Sciences under Grant No.2019050.

Appendix A. Correlation coefficients of species thermophysical properties

References

- [1] K. Zhou, S. Yang, Emission reduction of China's steel industry: Progress and challenges, *Renewable and Sustainable Energy Reviews* 61 (2016) 319–327.
- [2] S. K. Dutta, Y. B. Chokshi, *Basic concepts of Iron and steel making*, Springer Nature, 2020.
- [3] R. K. Soni, E. Chinthapudi, S. K. Tripathy, M. Bose, P. S. Goswami, Review on the chemical reduction modelling of hematite iron ore to magnetite in fluidized bed reactor, *Reviews in Chemical Engineering* (2022) 1–44.

Table A1: Correlation coefficients of the standard enthalpy with temperature.

Species	Temperature (K)	a_1	a_2	a_3	a_4	a_5	a_6
H ₂	298~1000	2.3443	7.98e-3	-1.95e-5	2.02e-8	-7.38e-12	-9.179e2
	1000~6000	2.9328	8.27e-4	-1.46e-7	1.54e-11	-6.89e-16	-8.131e2
H ₂ O	373~1000	4.1986	-2.04e-3	6.52e-6	-5.49e-9	1.77e-12	-3.03e4
	1000~6000	2.677	2.97e-3	-7.74e-7	9.44e-11	-4.27e-15	-2.989e4
N ₂	298~1000	3.531	-1.24e-4	-5.03e-7	2.44e-9	-1.41e-12	-1.047e3
	1000~6000	2.9526	1.40e-3	-4.93e-7	7.86e-11	-4.61e-15	-9.239e2
Fe ₂ O ₃	298~960	0.1522	6.71e-2	-1.13e-4	9.93e-8	-3.28e-11	-1.013e5
	960~1700	353.05	-0.9728	1.05e-3	-4.96e-7	8.74e-11	-1.96e5
Fe ₃ O ₄	298~850	4.8445	4.39e-2	5.25e-5	-2.21e-7	1.75e-10	-1.38e5
	850~1870	88.431	-0.149	1.26e-4	-4.7e-8	6.79e-12	-1.621e5
FeO	298~1000	5.3195	2.21e-3	1.07e-6	-2.79e-9	1.33e-12	-3.441e4
	1000~1650	5.8316	1.43e-3	-9.32e-8	-6.6e-12	-2.25e-14	-3.457e4
Fe	298~1000	2.4134	-1.58e-3	2.15e-5	-3.8e-8	2.20e-11	-774.38
	1000~1042	4690.8	-9.91	2.69e-3	5.54e-6	-3.02e-9	-1.415e6
	1042~1184	659.68	-1.14	4.96e-4	0	0	-2.52e5
	1184~1665	61.011	-0.161	1.68e-4	-7.75e-8	1.33e-11	-1.65e4

Table A2: Correlation coefficients of the gas viscosities with temperature.

Species	Temperature (K)	a_1	a_2	a_3
H ₂	298~2000	2.85e-6	2.16e-8	-3.78e-12
H ₂ O	373~1350	-4.44e-6	4.52e-8	-3.20e-12
N ₂	298~2000	7.86e-6	3.87e-8	-5.11e-12

Table A3: Correlation coefficients of the gas thermal conductivity coefficients with temperature.

Species	Temperature (K)	a_1	a_2	a_3	a_4	a_5
H ₂	298~2000	3.07e-3	8.09e-4	-8.52e-7	7.2e-10	-2.21e-13
H ₂ O	373~1350	6.84e-3	6.25e-6	1.31e-7	-5.99e-11	1.12e-14
N ₂	298~2000	2.51e-3	8.92e-5	-4.00e-8	1.62e-11	-2.61e-15

- [4] L. Lu, J. Pan, D. Zhu, Quality requirements of iron ore for iron production, in: *Iron Ore*, Elsevier, 2015, pp. 475–504.
- [5] T. Sun, Y. Shen, J. Jia, Gas cleaning and hydrogen sulfide removal for corex coal gas by sorption enhanced catalytic oxidation over recyclable activated carbon desulfurizer, *Environmental science & technology* 48 (4) (2014) 2263–2272.
- [6] S.-H. Yi, M.-E. Choi, D.-H. Kim, C.-K. Ko, W.-I. Park, S.-Y. Kim, Finex® as an environmentally sustainable ironmaking process, *Ironmaking & Steelmaking* 46 (7) (2019) 625–631.
- [7] S.-J. Jeong, System dynamics approach for the impacts of finex technology and carbon taxes on steel demand: Case study of the posco, *International Journal of Precision Engineering and Manufacturing-Green Technology* 2 (2015) 85–93.
- [8] M. Kwauk, H. Li, *Handbook of fluidization*, Chemical Industry Press Beijing, 2008.
- [9] S. He, H. Sun, C. Hu, J. Li, Q. Zhu, H. Li, Direct reduction of fine iron ore concentrate in a conical fluidized bed, *Powder Technology* 313 (2017) 161–168.
- [10] J. Brown, D. Campbell, A. Saxton, J. Carr Jr, FIOR-the Esso fluid iron ore direct reduction process, *JOM* 18 (2) (1966) 237–242.
- [11] T. Battle, U. Srivastava, J. Kopfle, R. Hunter, J. McClelland, The direct reduction of iron, in: *Treatise on process metallurgy*, Elsevier, 2014, pp. 89–176.
- [12] F. Plaul, C. Böhm, J. Schenk, Fluidized-bed technology for the production of iron products for steelmaking, *Journal of the Southern African Institute of Mining and Metallurgy* 109 (2) (2009) 121–128.
- [13] Y. Yu, W. Chen, Application of flash magnetizing roasting technique in beneficiation of siderite and limonite, in: *The 2010 international symposium on project management*, 2010, pp. 13–17.
- [14] J.-w. Yu, Y.-x. Han, Y.-j. Li, P. Gao, Growth behavior of the magnetite phase in the reduction of hematite via a fluidized bed, *International Journal of Minerals, Metallurgy, and Materials* 26 (2019) 1231–1238.
- [15] Y.-j. Li, R. Wang, Y.-x. Han, X.-c. Wei, Phase transformation in suspension roasting of oolitic hematite ore, *Journal of Central South University* 22 (12) (2015) 4560–4565.
- [16] Z. Du, Q. Zhu, Y. Yang, C. Fan, F. Pan, H. Sun, Z. Xie, The role of MgO powder in preventing defluidization during fluidized bed reduction of fine iron ores with different iron valences, *steel research international* 87 (12) (2016) 1742–1749.
- [17] Z. Du, Y. Ge, F. Liu, C. Fan, F. Pan, Effect of different modification methods on fluidized bed hydrogen reduction of cohesive iron ore fines, *Powder Technology* 400 (2022) 117226.
- [18] Z. Du, J. Liu, F. Liu, F. Pan, Relationship of particle size, reaction and sticking behavior of iron ore fines toward efficient fluidized bed reduction, *Chemical Engineering Journal* 447 (2022) 137588.
- [19] Z. Du, Q. Zhu, C. Fan, F. Pan, Z. Xie, Enhanced effect and mechanism of Fe₂O₃ on cao for defluidization inhibition during fluidized bed reduction of iron ore fines, *Powder Technology* 313 (2017) 82–87.
- [20] D. Spreitzer, J. Schenk, Iron ore reduction by hydrogen using a laboratory scale fluidized bed reactor: Kinetic investigation—experimental setup and method for determination, *Metallurgical and materials transactions B* 50 (2019) 2471–2484.
- [21] D. Spreitzer, J. Schenk, Fluidization behavior and reducibility of iron ore fines during hydrogen-induced fluidized bed reduction, *Particuology* 52 (2020) 36–46.
- [22] Y. Zhong, J. Gao, Z. Guo, A model for solid surface viscosity of iron powders at high temperature: Influence of particle size distribution, *Powder Technology* 335 (2018) 371–374.
- [23] M. Komatina, H. W. GUDENAU, The sticking problem during direct reduction of fine iron ore in the fluidized bed, *Metallurgical and Materials Engineering*.
- [24] C. Lei, G. Zhang, Q. Zhu, Z. Xie, Optimization of carbon deposition process during the pre-reduction of fine iron ore in a fluidized bed, *Powder Technology* 296 (2016) 79–86.
- [25] C. Lei, Q. Zhu, H. Li, Experimental and theoretical study on the fluidization behaviors of iron powder at high temperature, *Chemical Engineering Science* 118 (2014) 50–59.
- [26] Y. Zhong, Z. Wang, Z. Guo, Q. Tang, Defluidization behavior of iron powders at elevated temperature: Influence of fluidizing gas and particle adhesion, *Powder Technology* 230 (2012) 225–231.
- [27] L. Holappa, Recent achievements in iron and steel technology., *Journal of Chemical Technology & Metallurgy* 52 (2) (2017) 159–167.
- [28] R. An, B. Yu, R. Li, Y.-M. Wei, Potential of energy savings and CO₂ emission reduction in China's iron and steel industry, *Applied energy* 226 (2018) 862–880.
- [29] F. Patisson, O. Mirgaux, Hydrogen ironmaking: How it works, *Metals* 10 (7) (2020) 922.
- [30] J. Shi, E. Donskoi, D. S. McElwain, L. J. Wibberley, Modelling the reduction of an iron ore-coal composite pellet with conduction and convection in an axisymmetric temperature field, *Mathematical and computer modelling* 42 (1-2) (2005) 45–60.
- [31] M. Valipour, Mathematical modeling of a non-catalytic gas-solid reaction: hematite pellet reduction with syngas, *Scientia Iranica* 16 (2) (2009) 108–124.
- [32] H. Tang, Z. Guo, K. Kitagawa, Simulation study on performance of z-path moving-fluidized bed for gaseous reduction of iron ore fines, *ISIJ international* 52 (7) (2012) 1241–1249.
- [33] S. Natsui, T. Kikuchi, R. O. Suzuki, Numerical analysis of carbon monoxide–hydrogen gas reduction of iron ore in a packed bed by an euler–lagrange approach, *Metallurgical and Materials Transactions B* 45 (2014) 2395–2413.
- [34] S. Nouri, H. A. Ebrahim, E. Jamshidi, Simulation of direct reduction reactor by the grain model, *Chemical Engineering Journal* 166 (2) (2011) 704–709.
- [35] Z. G. Ariyan, V. Mohammad Sadegh, B. Mojtaba, Numerical analysis of complicated heat and mass transfer inside a wustite pellet during reducing to sponge iron by H₂ and CO gaseous mixture, *Journal of Iron and Steel Research International* 23 (11) (2016) 1142–1150.
- [36] M. E. Kinaci, T. Lichtenegger, S. Schneiderbauer, Direct reduction of iron-ore in fluidized beds, in: *Computer Aided Chemical Engineering*, Vol. 43, Elsevier, 2018, pp. 217–222.
- [37] M. Kinaci, T. Lichtenegger, S. Schneiderbauer, A CFD-DEM model for the simulation of direct reduction of iron-ore in fluidized beds, *Chemical Engineering Science* 227 (2020) 115858.
- [38] S. Schneiderbauer, M. E. Kinaci, F. Hauenberger, Computational fluid dynamics simulation of iron ore reduction in industrial-scale fluidized beds, *steel Research International* 91 (12) (2020) 2000232.

- [39] Z.-w. Wan, J.-y. Huang, G.-m. Zhu, Q.-y. Xu, Numerical simulation of the operating conditions for the reduction of iron ore powder in a fluidized bed based on the CPFD method, *Processes* 10 (9) (2022) 1870.
- [40] J. G. Rosser, Investigation of jamming phenomenon in a DRI furnace pellet feed system using the discrete element method and computational fluid dynamics, Ph.D. thesis, Purdue University Graduate School (2023).
- [41] E. Dianyu, Validation of CFD-DEM model for iron ore reduction at particle level and parametric study, *Particuology* 51 (2020) 163–172.
- [42] D. Xu, S. Wang, Y. Shen, Coarse-grained rCFD-DEM analysis of coke gasification and iron ore reduction in the shaft region of an ironmaking blast furnace, *Powder Technology* 408 (2022) 117706.
- [43] O. Levenspiel, *Chemical Reaction Engineering*, John Wiley & Sons, 1998.
- [44] M. E. Kinaci, T. Lichtenegger, S. Schneiderbauer, Modelling of chemical reactions in metallurgical processes, in: *Proceedings of the 12th International Conference on Computational Fluid Dynamics in the Oil & Gas, Metallurgical and Process Industries*, SINTEF Academic Press, 2017.
- [45] D. Spreitzer, J. Schenk, Reduction of iron oxides with hydrogen—a review, *Steel Research International* 90 (10) (2019) 1900108.
- [46] R. Spitzer, F. Manning, W. Philbrook, Generalized model for the gaseous, topochemical reduction of porous hematite spheres, *AIME Met Soc Trans* 236 (12) (1966) 1715–1724.
- [47] W. Zhang, J. Zhang, Q. Li, Y. He, B. Tang, M. Li, Z. Zhang, Z. Zou, Thermodynamic analyses of iron oxides redox reactions, in: *Proceedings of the 8th Pacific Rim International Congress on Advanced Materials and Processing*, Springer, 2013, pp. 777–789.
- [48] Y. Takenaka, Y. Kimura, K. Narita, D. Kaneko, Mathematical model of direct reduction shaft furnace and its application to actual operations of a model plant, *Computers & chemical engineering* 10 (1) (1986) 67–75.
- [49] D. Gunn, Transfer of heat or mass to particles in fixed and fluidised beds, *International Journal of Heat and Mass Transfer* 21 (4) (1978) 467–476.
- [50] S. Li, F. Xin, L. Li, *Reaction Engineering*, Butterworth-Heinemann, 2017.
- [51] E. N. Fuller, P. D. Schettler, J. C. Giddings, New method for prediction of binary gas-phase diffusion coefficients, *Industrial & Engineering Chemistry* 58 (5) (1966) 18–27.
- [52] C. Wilke, P. Chang, Correlation of diffusion coefficients in dilute solutions, *AIChE Journal* 1 (2) (1955) 264–270.
- [53] N. Wakao, J. Smith, Diffusion in catalyst pellets, *Chemical Engineering Science* 17 (11) (1962) 825–834.
- [54] B. Lan, J. Xu, P. Zhao, Z. Zou, Q. Zhu, J. Wang, Long-time coarse-grained CFD-DEM simulation of residence time distribution of polydisperse particles in a continuously operated multiple-chamber fluidized bed, *Chemical Engineering Science* 219 (2020) 115599.
- [55] D. Gidaspow, *Multiphase flow and fluidization: continuum and kinetic theory descriptions*, Academic press, 1994.
- [56] G. H. Ganser, A rational approach to drag prediction of spherical and nonspherical particles, *Powder Technology* 77 (2) (1993) 143–152.
- [57] L. Hua, H. Zhao, J. Li, J. Wang, Q. Zhu, Eulerian-Eulerian simulation of irregular particles in dense gas-solid fluidized beds, *Powder Technology* 284 (2015) 299–311.
- [58] B. Lan, P. Zhao, J. Xu, B. Zhao, M. Zhai, J. Wang, CFD-DEM-IBM simulation of particle drying processes in gas-fluidized beds, *Chemical Engineering Science* 255 (2022) 117653.
- [59] J. Xu, X. Liu, S. Hu, W. Ge, Virtual process engineering on a three-dimensional circulating fluidized bed with multiscale parallel computation, *Journal of Advanced Manufacturing and Processing* 1 (1-2) (2019) e10014.
- [60] G. K. Batchelor, R. O'Brien, Thermal or electrical conduction through a granular material, *Proceedings of the Royal Society of London. A. Mathematical and Physical Sciences* 355 (1682) (1977) 313–333.
- [61] D. Rong, M. Horio, DEM simulation of char combustion in a fluidized bed, in: *Second International Conference on CFD in the Minerals and Process Industries CSIRO*, Melbourne, Australia, 1999, pp. 65–70.
- [62] P. Zhao, J. Xu, X. Liu, W. Ge, J. Wang, A computational fluid dynamics-discrete element-immersed boundary method for cartesian grid simulation of heat transfer in compressible gas–solid flow with complex geometries, *Physics of Fluids* 32 (10) (2020) 103306.
- [63] Z. Zhou, A. Yu, P. Zulli, Particle scale study of heat transfer in packed and bubbling fluidized beds, *AIChE Journal* 55 (4) (2009) 868–884.
- [64] J. Musser, M. Syamlal, M. Shahnam, D. Huckaby, Constitutive equation for heat transfer caused by mass transfer, *Chemical Engineering Science* 123 (2015) 436–443.
- [65] A. Burcat, B. Ruscic, Third millennium ideal gas and condensed phase thermochemical database for combustion (with update from active thermochemical tables), Tech. rep., Argonne National Lab.(ANL), Argonne, IL (United States) (2005).
- [66] M. Mehrabadi, S. Tenneti, R. Garg, S. Subramaniam, Pseudo-turbulent gas-phase velocity fluctuations in homogeneous gas–solid flow: fixed particle assemblies and freely evolving suspensions, *Journal of Fluid Mechanics* 770 (2015) 210–246.
- [67] C. Peng, B. Kong, J. Zhou, B. Sun, A. Passalacqua, S. Subramaniam, R. Fox, Implementation of pseudo-turbulence closures in an eulerian–eulerian two-fluid model for non-isothermal gas–solid flow, *Chemical Engineering Science* 207 (2019) 663–671.
- [68] B. Sun, S. Tenneti, S. Subramaniam, Modeling average gas–solid heat transfer using particle-resolved direct numerical simulation, *International Journal of Heat and Mass Transfer* 86 (2015) 898–913.
- [69] H. R. Norouzi, R. Zarghami, R. Sotudeh-Gharebagh, N. Mostoufi, *Coupled CFD-DEM modeling: formulation, implementation and application to multiphase flows*, John Wiley & Sons, 2016.
- [70] L. Lu, J. Xu, W. Ge, Y. Yue, X. Liu, J. Li, EMMS-based discrete particle method (EMMS-DPM) for simulation of gas-solid flows, *Chemical Engineering Science* 120 (2014) 67–87.
- [71] L. Lu, J. Xu, W. Ge, G. Gao, Y. Jiang, M. Zhao, X. Liu, J. Li, Computer virtual experiment on fluidized beds using a coarse-grained discrete particle method-EMMS-DPM, *Chemical Engineering Science* 155 (2016) 314–337.
- [72] B. Lan, J. Xu, Z. Liu, J. Wang, Simulation of scale-up effect of particle residence time distribution characteristics in continuously operated dense-phase fluidized beds, *CIESC Journal* 72 (2021) 521–533.
- [73] L. Lu, A. Morris, T. Li, S. Benyahia, Extension of a coarse grained particle method to simulate heat transfer in fluidized beds, *International Journal of Heat and Mass Transfer* 111 (2017) 723–735.
- [74] C. Hu, Y. He, D. Liu, S. Sun, D. Li, Q. Zhu, J. Yu, Advances in mineral processing technologies related to iron, magnesium, and lithium, *Reviews in Chemical Engineering* 36 (1) (2019) 107–146.
- [75] J. Yu, L. Lu, Y. Xu, X. Gao, M. Shahnam, W. Rogers, Coarse-grained CFD-DEM simulation and the design of an industrial-scale coal gasifier,

- Industrial & Engineering Chemistry Research 61 (1) (2021) 866–881.
- [76] S. Du, J. Wang, Y. Yu, Q. Zhou, Coarse-grained CFD-DEM simulation of coal and biomass co-gasification process in a fluidized bed reactor: Effects of particle size distribution and operating pressure, *Renewable Energy* 202 (2023) 483–498.
- [77] M. Doble, *Perry's Chemical Engineers' Handbook*, McGraw-Hill, New York, US.
- [78] A. Niksiar, A. Rahimi, Design of a moving bed reactor for the production of uranium tetrafluoride based on mathematical modeling, *Chemical engineering science* 65 (10) (2010) 3147–3157.
- [79] P. Zhao, J. Xu, W. Ge, J. Wang, A CFD-DEM-IBM method for Cartesian grid simulation of gas-solid flow in complex geometries, *Chemical Engineering Journal* 389 (2020) 124343.
- [80] P. Zhao, J. Xu, B. Zhao, D. Li, J. Wang, Cartesian grid simulation of reacting gas-solid flow using CFD-DEM-IBM method, *Powder Technology* 407 (2022) 117651.
- [81] P. Zhao, J. Xu, Q. Chang, W. Ge, J. Wang, Euler-Lagrange simulation of dense gas-solid flow with local grid refinement, *Powder Technology* 399 (2022) 117199.
- [82] B. Lan, P. Zhao, J. Xu, B. Zhao, M. Zhai, J. Wang, The critical role of scale resolution in CFD simulation of gas-solid flows: A heat transfer study using CFD-DEM-IBM method, *Chemical Engineering Science* 266 (2023) 118268.
- [83] S. Li, P. Zhao, J. Xu, L. Zhang, J. Wang, Direct comparison of CFD-DEM simulation and experimental measurement of Geldart A particles in a micro-fluidized bed, *Chemical Engineering Science* 242 (2021) 116725.
- [84] S. Li, P. Zhao, J. Xu, L. Zhang, J. Wang, CFD-DEM simulation of polydisperse gas-solid flow of Geldart A particles in bubbling micro-fluidized beds, *Chemical Engineering Science* 253 (2022) 117551.
- [85] A. Heidari, N. Niknahad, M. Iljana, T. Fabritius, A review on the kinetics of iron ore reduction by hydrogen, *Materials* 14 (24) (2021) 7540.
- [86] R. Nicolle, A. Rist, The mechanism of whisker growth in the reduction of wüstite, *Metallurgical Transactions B* 10 (1979) 429–438.
- [87] D. Spreitzer, Development of characterization methods for the evaluation of the kinetic behavior and the fluidization of iron ore fines during hydrogen-induced fluidized bed reduction, Ph.D. thesis, Montan University (2020).